Electronic Supplementary Information (ESI) for *Energy Advances*.

Supplementary Material for

"Purity-Constrained TVSA Modeling of Lewatit VPOC 1065 for Direct Air Capture: Bridging Cured Thermodynamics, Process Design and Geometrical Analysis"

Mattia Galanti, Kiia Kaaresvirta, Ivo Roghair, Martin van Sint Annaland

Department of Chemical Engineering and Chemistry, Eindhoven University of Technology, Eindhoven, 5600MB, The Netherlands.
E-mail: M.v.SintAnnaland@tue.nl

S1 Thermodynamics

S1.1 Dry CO_2 complete dataset Toth fit

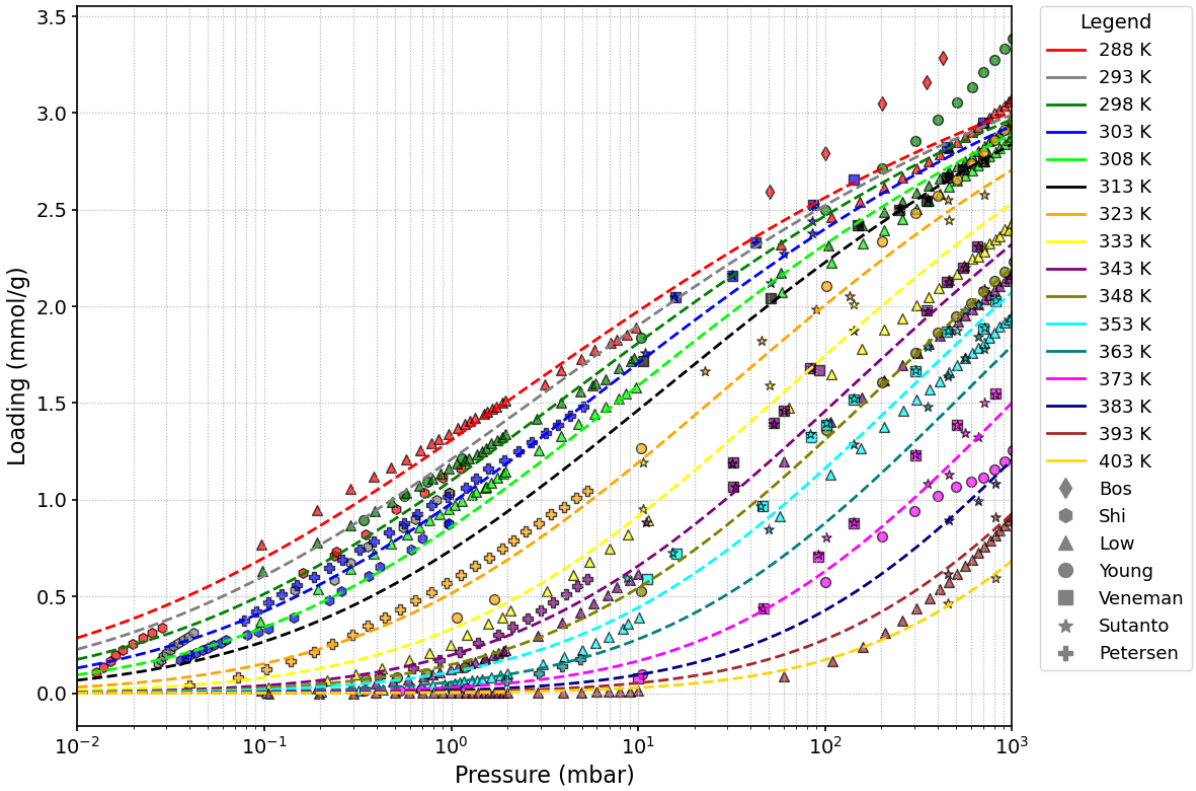

Figure S1: Toth fit for dry CO_2 isotherm using all the data gathered from literature.

When all sources are considered, the fit is unsatisfactory due to inconsistencies across datasets. Data reported by Shi et al. at ultra-low pressures (0.01 mbar to 0.1 mbar) deviates strongly from other studies. At higher pressures, measurements by Low et al. systematically underestimate the adsorption loading compared to other sources, whereas Young et al. shows good agreement with the majority of datasets.

0.01–10 mbar As shown in Fig. S2, in the pressure region 0.01–1 mbar, the residuals from Low, Young and Petersen are symmetrically distributed around zero with comparable variance, indicating that both datasets are internally consistent and unbiased with respect to the Toth model. In contrast, the measurements from Shi et al. exhibit a systematic negative bias, with residuals predominantly between -0.20 and -0.10 mmol g^{-1}. This consistent underestimation suggests that the discrepancy is not due to random scatter but to a structural deviation between Shi's data and the rest of the dataset. The clustered negative residuals at low loadings and the mismatch in curvature imply that either (i) the Toth functional form cannot reproduce the behavior under such dilute conditions, or (ii) experimental uncertainties dominate in this pressure regime. To preserve the internal consistency of the joint fit, data from Shi et al. were therefore excluded from the fitting procedure.

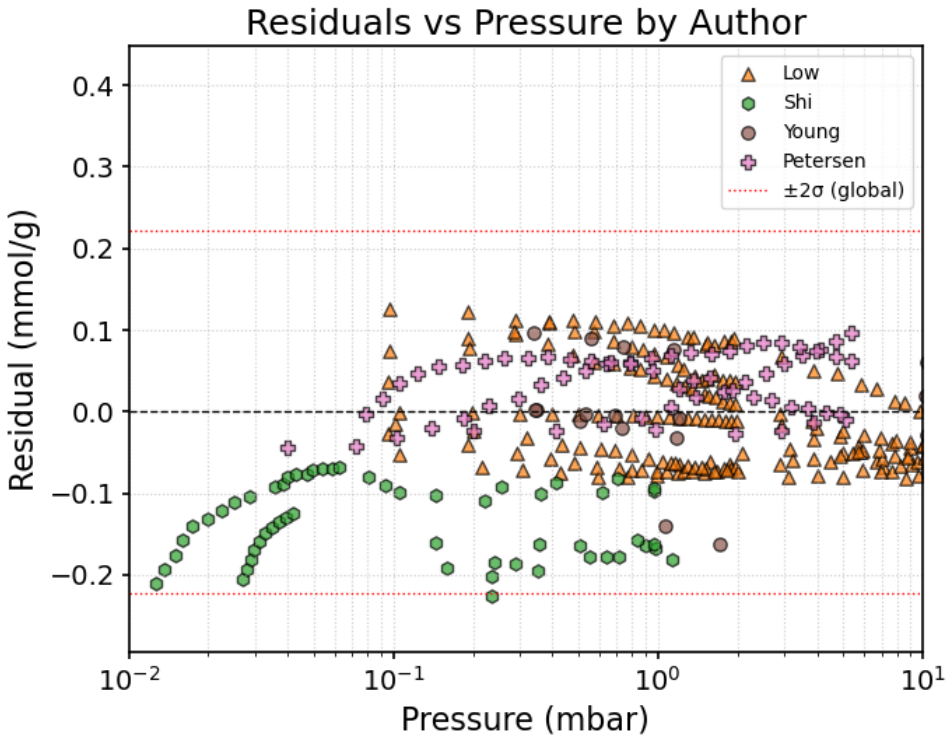

Figure S2: Residuals of the Toth model fit in the low-pressure region (0.01–10 mbar) for different literature datasets. Each color and marker corresponds to a specific data source. The red dotted lines denote the global $\pm 2\sigma$ confidence bounds computed over all data.

10–1000 mbar As shown in Fig. S3, in the 10-1000 mbar pressure range, the residuals reveal a systematic divergence between Low and the other datasets. While Young, Sutanto, and Veneman exhibit mutually coherent behavior (residuals that are predominantly near zero to slightly positive and broadly consistent with each other), Low displays a persistent negative offset. If the mismatch arose solely from limitations of the Toth functional form, a similar residual structure would be expected across all sources. The fact that the deviation is localized in a single dataset points instead to dataset-specific bias.

To quantify the degree of consistency between sources, pairwise Kolmogorov–Smirnov (KS) tests were performed on the residual distributions in the 10–1000 mbar range. The KS statistic (D) measures the maximum distance between the cumulative distribution functions (CDFs) of two samples: values close to zero indicate statistically indistinguishable distributions (datasets behave coherently within model uncertainty), whereas values approaching one indicate complete distributional separation. The associated p-value represents the probability of observing a distance at least as large as D if the two samples were drawn from the same underlying distribution. In practice, datasets are considered statistically consistent when $D < 0.3$ and $p > 0.05$, while larger D and smaller p indicate significant distributional differences.

The results show that Low differs strongly from each of Bos, Young, Sutanto, and Veneman (D = 0.68–1.00, $p < 10^{-3}$), confirming that its residual distribution is statistically distinct from all others. Conversely, Young vs. Sutanto ($D = 0.2250$, $p = 0.1280$), Sutanto vs. Veneman ($D = 0.1549$, $p = 0.4727$), and Veneman vs. Young ($D = 0.3299$, $p = 0.0200$) are broadly consistent with one another, matching their visual agreement in Fig. S3. This combination of visual and statistical evidence supports the exclusion of the

high-pressure subset from Low et al. to avoid biasing the global fit, while retaining Low and Young in the low-pressure regime where they cross-validate each other.

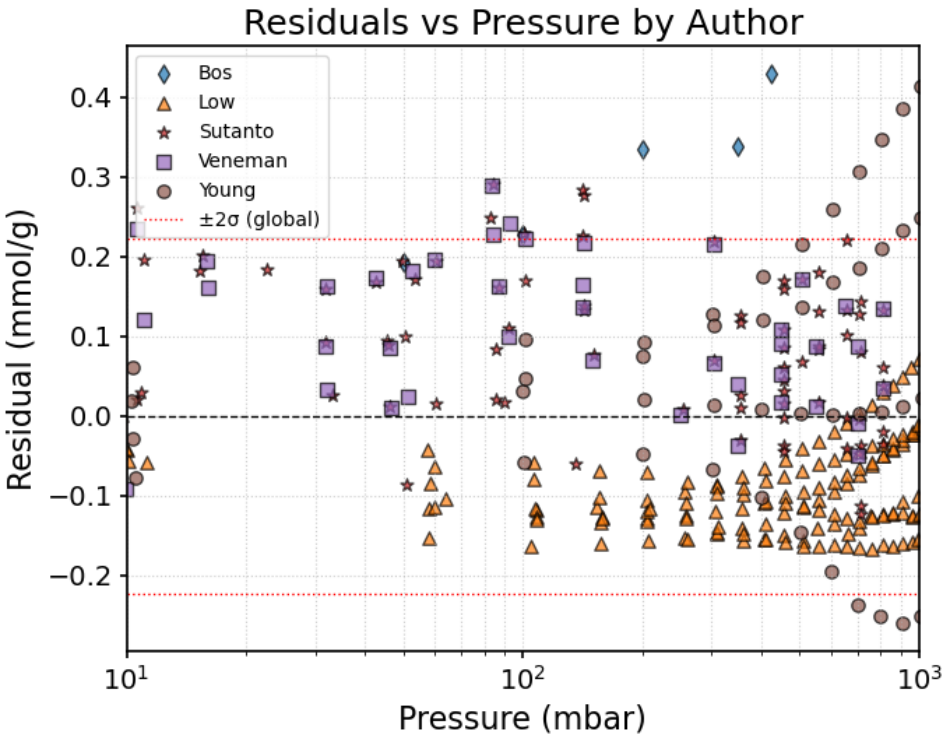

Figure S3: Residuals of the Toth fit in the 10–1000 mbar pressure region, grouped by data source. Each color and marker corresponds to a specific dataset, consistent with the main text. The red dotted lines show the global $\pm 2\sigma$ confidence band (computed from all data). Residuals from Low systematically fall below zero, while Young, Sutanto, and Veneman form a mutually coherent group within model uncertainty.

S1.2 Fitting metrics definition

Given a dataset of N experimental points with measured values q_i^{exp} and model-predicted values q_i^{mod}, the metrics are defined as follows:

$$\text{RMSE} = \sqrt{\frac{1}{N}\sum_{i=1}^{N}\left(q_i^{\text{exp}} - q_i^{\text{mod}}\right)^2} \tag{S1}$$

$$\text{MAE} = \frac{1}{N}\sum_{i=1}^{N}\left|q_i^{\text{exp}} - q_i^{\text{mod}}\right| \tag{S2}$$

(S3)

where $\bar{q}^{\text{exp}}$ denotes the mean of the experimental values.

- RMSE penalizes larger deviations more strongly than MAE due to the squaring of residuals, scaled back to unit with root.
- MAE represents the average absolute deviation and is less sensitive to outliers.

S1.3 H_2O isotherm: data and fitting

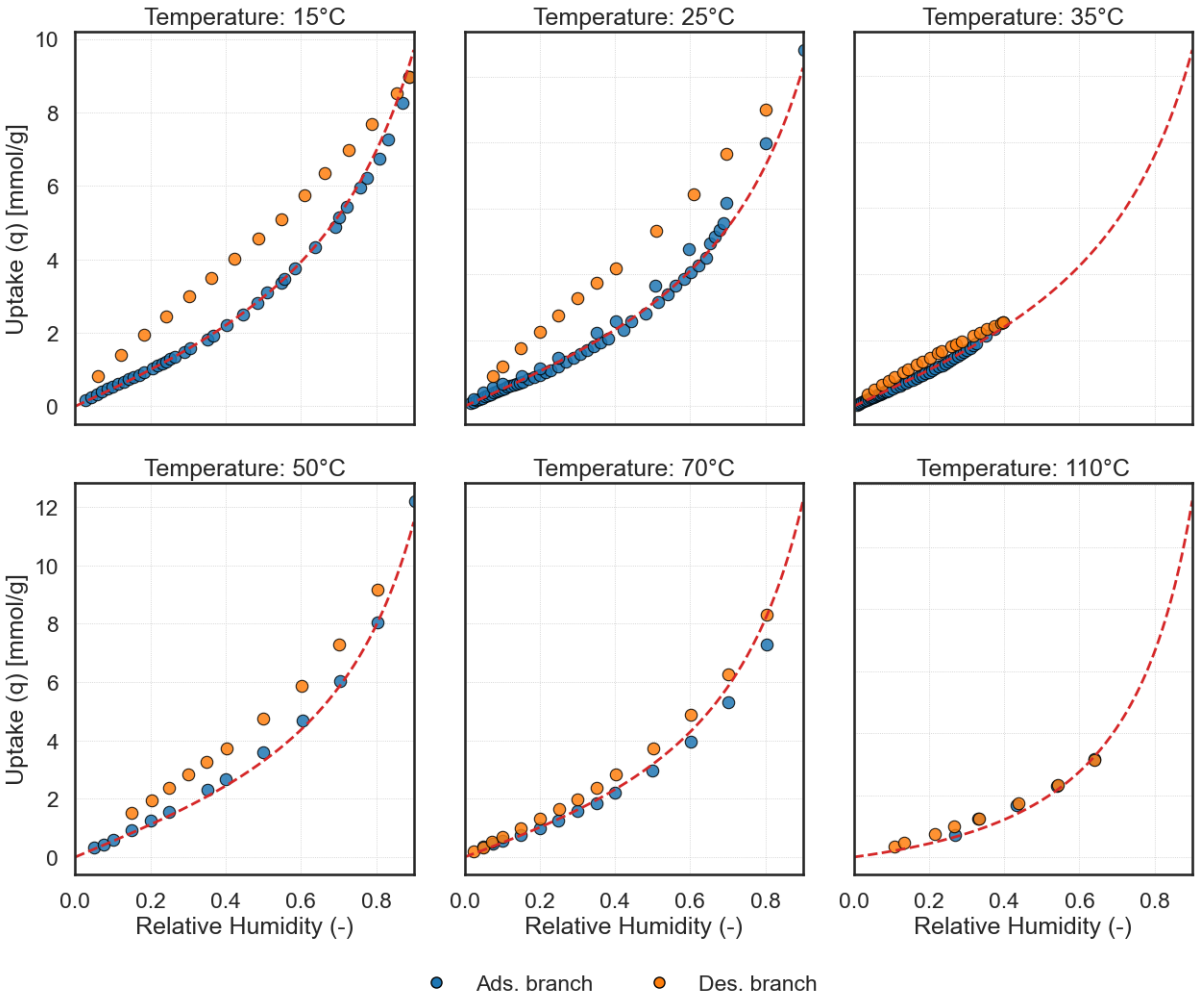

Figure S4: Adsorption (blue) and desorption (orange) branches of the H_2O isotherms on Lewatit VPOC 1065. The red dashed lines refers to the GAB isotherm fit. The GAB model was fitted only to the adsorption branches.

S1.4 Binary CO_2-H_2O isotherm data

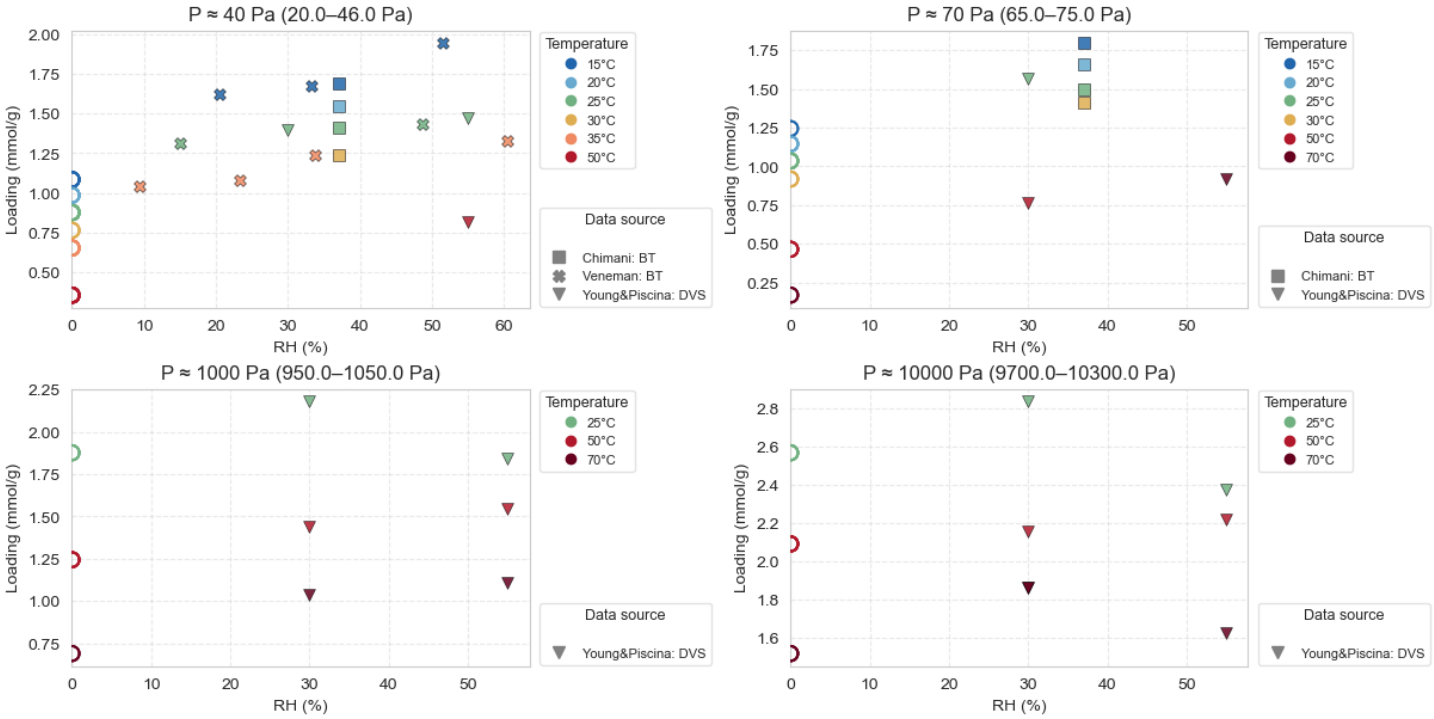

Figure S5: Collected and curated binary CO_2-H_2O isotherm data for Lewatit VPOC 1065, displayed in pressure bins for visualization. The dry reference is highlighted.

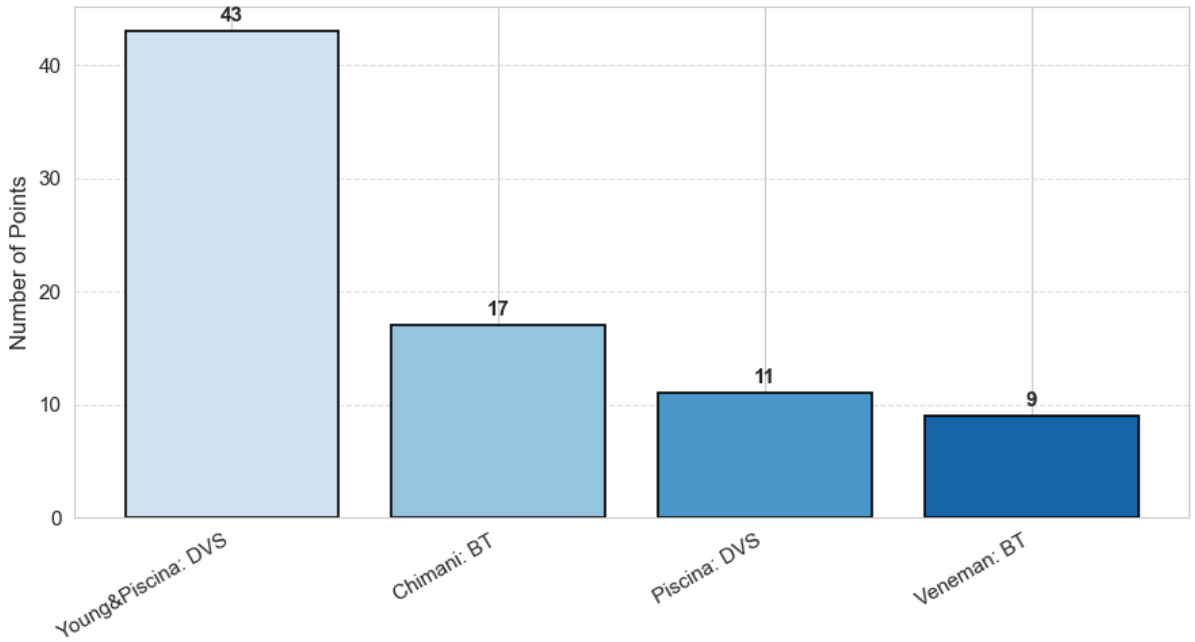

Figure S6: Author counts for co-adsorption data.

S1.5 Stampi-Bombelli model fitting of co-adsorption dataset

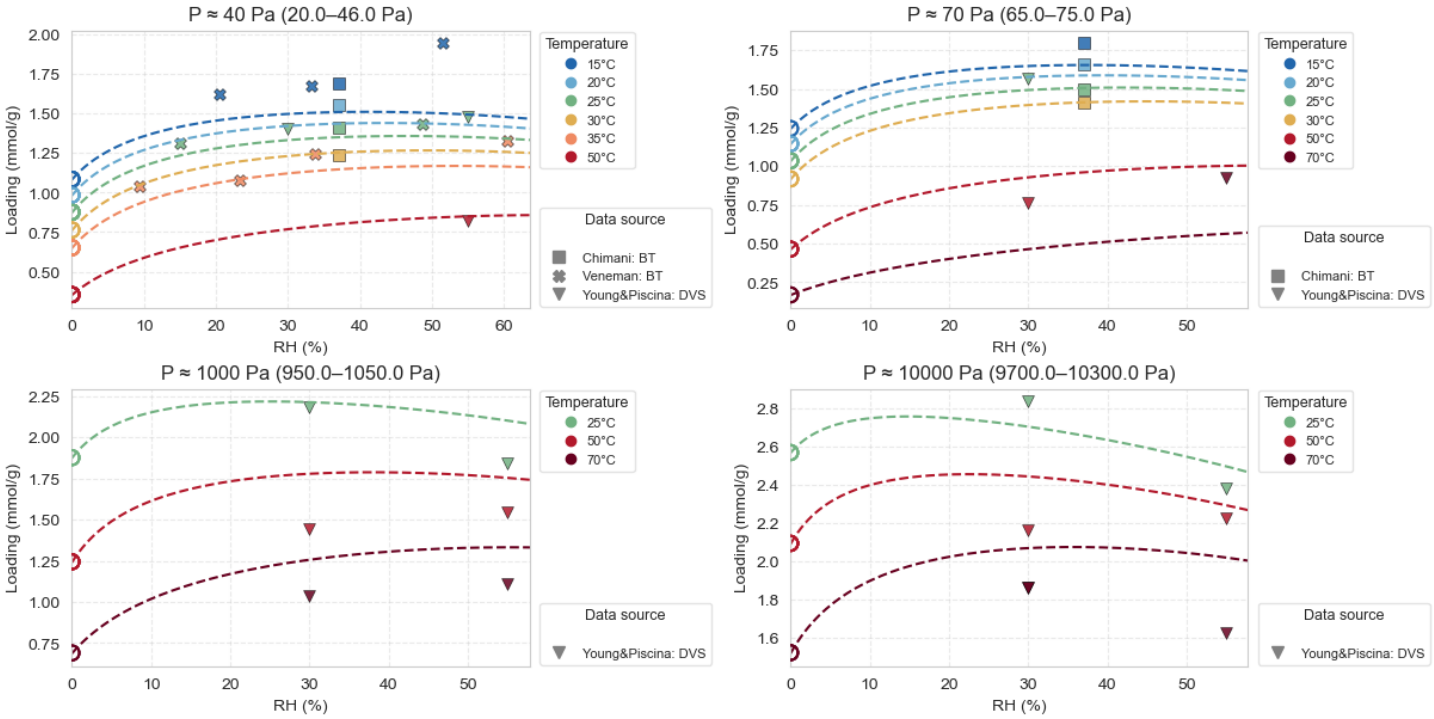

Figure S7: Fit of the Stampi-Bombelli (SB) model to the curated co-adsorption dataset. The SB model captures the general trend but shows poorer agreement.

S1.6 Stampi-Bombelli model comparison

Table S1: Key performance indicators comparing the base case (no co-adsorption) and the Stampi-Bombelli (SB) co-adsorption model.

KPI	No co-adsorption	SB co-adsorption
Equivalent work [MJ/kg CO_2]	4.076	4.905
Productivity [kgCO_2/m^3/day]	38.55	31.45
Cyclic working capacity [mol/kg]	0.6724	0.5189
Total Yield [%]	57.99	38.50

We tested the SB co-adsorption implementation and compared it with the dry implementation as described in Sec.3 of the main text. The productivity and equivalent work KPIs definition can be found in the main text. For this additional test, new performance indicators were defined:

- Cyclic working capacity: difference between the sorbent loading at the end of adsorption and after desorption, at cyclic steady state.

$$\Delta q_{wc} = q_{ads} - q_{des} \tag{S4}$$

- Total yield: fraction of the total amount of CO_2 present in the adsorber at the end of adsorption that is actually desorbed.

$$Yield_{tot} = \frac{\Delta m^{des}_{CO_2}}{m^{ads}_{CO_2}} \tag{S5}$$

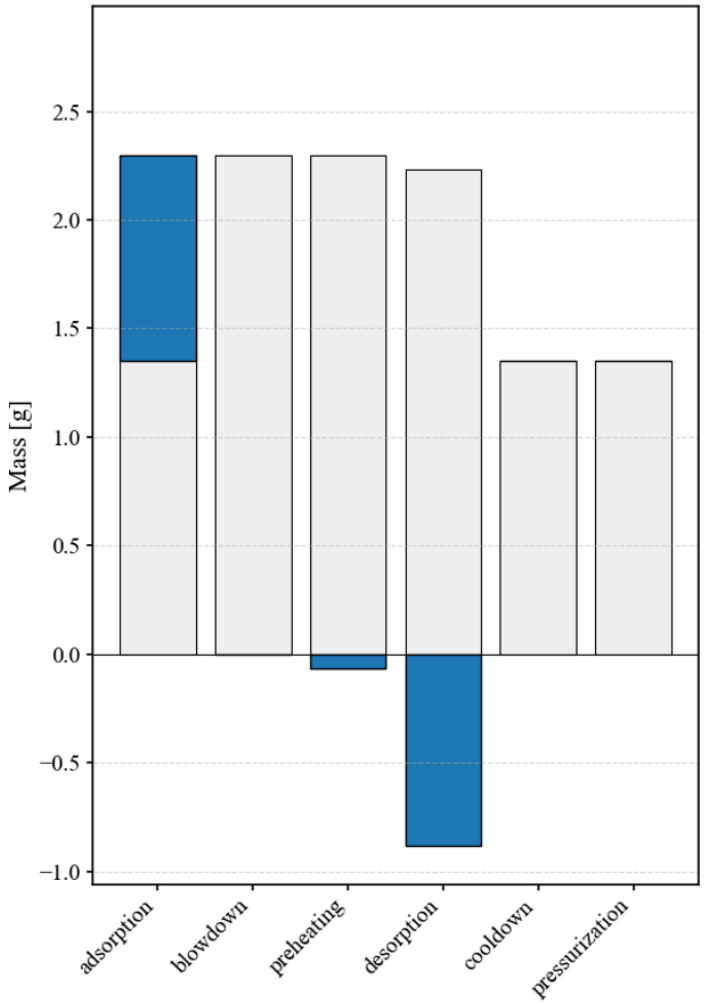

Figure S8: Stepwise mass balance for the Stampi-Bombelli (SB) model extracted from a test simulation. For each cycle step, the mass change is shown in blue (positive values correspond to adsorption, negative values to desorption), while the initial mass at the beginning of the step is shown in gray.

As shown in Table S1, the SB model predicts systematically poorer performance across all KPIs when co-adsorption is considered compared to the dry case. As highlighted by Young et al. [1], this limitation is intrinsic to the SB formulation: the model does not adequately describe CO_2 desorption, resulting in a significant fraction of CO_2 being retained within the sorbent rather than being released and collected. This behavior is illustrated in Fig. S8, where the mass change at each step is shown in blue and the initial mass in gray. The figure clearly indicates that the SB model enforces inefficient desorption: only a small fraction of CO_2 is expelled, while the majority remains trapped inside the adsorber. This arises from the SB formulation, which couples q_{CO_2} to q_{H_2O} via the temperature-dependent parameters q_m and b. Since q_{H_2O} is described by the GAB isotherm and remains relatively insensitive to temperature, the model predicts persistently high q_{H_2O} values even at elevated temperatures. This, in turn, artificially enhances q_{CO_2} during the desorption step, preventing the expected decrease in loading and leading to excessive residual CO_2 within the bed.

S2 Process Modeling

S2.1 Definitions and parameters

In order to improve the numerical stability of the model, it is often convenient to rewrite the governing equations in non-dimensional form. This approach reduces the number of physical parameters, highlights dominant physical effects through dimensionless groups, and ensures that all variables are on a comparable scale, which is critical when solving stiff systems numerically. The non-dimensional variables used in the main text are defined as follows:

$$\overline{p} = \frac{p}{p_{\text{ref}}}, \quad \overline{T} = \frac{T}{T_{\text{ref}}}, \quad \tau = \frac{t}{\tau_{\text{hyd}}} = \frac{t}{L/v_{\text{ref}}}, \quad Z = \frac{z}{L}, \quad \vec{v} = \frac{\vec{v}_{\text{dim}}}{v_{\text{ref}}}$$

Note that the gradient and divergence operator in the main text is evaluated on the non-dimensional space coordinate Z.

All the parameters describing the governing PDEs system in the main text are defined as follows:

- $\psi_{\text{ads},i} = \dfrac{(1-\varepsilon_b)}{\varepsilon_b}\dfrac{\rho_p}{c_{\text{tot,ref}}} q_{i,\text{eq,ref}}$: Dimensionless adsorption capacity for species i
- $\alpha_i = \tau_{\text{hyd}}\, k_{\text{LDF},i}$: Dimensionless mass transfer coefficient for species i
- $Pe_m = \dfrac{v_{\text{ref}} L_b}{D_{\text{ax}}}$: Mass Peclet number
- $Pe_h = \dfrac{v_{\text{ref}} L_b}{\lambda_{\text{ax}}}$: Heat Peclet number
- $\Omega_p = \dfrac{\varepsilon_b c_{\text{tot,ref}} R}{\rho_b c_{p,p}}$: Pressure coupling parameter in the energy balance
- $\Omega_c = \dfrac{\varepsilon_b c_{p,g} c_{\text{tot,ref}}}{\rho_b c_{p,p}}$: Convective heat transfer parameter
- $\Omega_k = \dfrac{1}{Pe_h \rho_b c_{p,p}}$: Effective thermal conductivity parameter
- $\psi_{\text{heat},i} = \dfrac{\Delta H_{ads,i} q_{i,\text{eq,ref}}}{c_{p,p} T_{\text{ref}}}$: Heat release parameter due to adsorption of species i
- $\Omega_w = \dfrac{a_{v,b} h_w \tau_{\text{hyd}}}{\rho_b c_{p,p}}$: Heat exchange parameter between gas and wall
- $\Omega_{kw} = \dfrac{\lambda_w}{\rho_w c_{p,w} v_{\text{ref}} L_b}$: Wall thermal conduction parameter
- $\Omega_w^{\text{int}} = \dfrac{2 R_b h_w \tau_{\text{hyd}}}{(\rho_w c_{p,w})(R_{b,\text{ext}}^2 - R_b^2)}$: Internal wall-to-gas heat exchange parameter
- $\Omega_w^{\text{ext}} = \dfrac{2 R_{b,\text{ext}} h_{\text{ext}} \tau_{\text{hyd}}}{(\rho_w c_{p,w})(R_{b,\text{ext}}^2 - R_b^2)}$: External wall-to-jacket heat exchange parameter

where ε_b is the bed porosity (−), ρ_p is the particle density (kg m^{-3}), $c_{\mathrm{tot,ref}}$ is the reference total molar concentration (mol m^{-3}), $q_{i,\mathrm{eq,ref}}$ is the reference equilibrium adsorption capacity of species i (mol kg^{-1}), $k_{\mathrm{LDF},i}$ is the linear driving force (LDF) mass transfer coefficient of species i (s^{-1}), L_b is the bed length (m), D_{ax} is the axial dispersion coefficient (m^2 s^{-1}), λ_{ax} is the effective axial thermal conductivity (W m^{-1} K^{-1}), R is the universal gas constant (J mol^{-1} K^{-1}), ρ_b is the bed density (kg m^{-3}), $c_{p,p}$ is the particle heat capacity (J kg^{-1} K^{-1}), $c_{p,g}$ is the gas-phase heat capacity (J mol^{-1} K^{-1}), $\Delta H_{ads,i}$ is the heat of adsorption of species i (J mol^{-1}), T_{ref} is the reference temperature (K), $a_{v,b}$ is the specific surface area per unit bed volume (m^2 m^{-3}), h_w is the wall-to-fluid heat transfer coefficient (W m^{-2} K^{-1}), λ_w is the wall thermal conductivity (W m^{-1} K^{-1}), ρ_w is the wall density (kg m^{-3}), $c_{p,w}$ is the wall heat capacity (J kg^{-1} K^{-1}), R_b is the bed inner radius (m), $R_{b,\mathrm{ext}}$ is the external wall radius (m), h_{ext} is the external heat transfer coefficient between wall and jacket (W m^{-2} K^{-1}), and v_{ref} is the reference interstitial velocity (m s^{-1}).

S2.2 Closure models and additional equations

S2.2.1 Pressure drop and axial velocity (Kozeny-Carman closure)

The axial gas velocity field is not treated as an independent unknown from the momentum balance. Under laminar conditions, the viscous contribution of the Ergun equation reduces to the Kozeny-Carman relation:

$$-\frac{\partial p}{\partial z} = \frac{150\,\mu}{d_p^2}\,\frac{(1-\varepsilon_b)^2}{\varepsilon_b^3}\,u(z,t) \tag{S6}$$

where p is the total gas pressure, μ is the gas mixture viscosity, d_p is the particle diameter, and ε_b is the bed void fraction. Therefore, once the pressure field is obtained from the total mass balance (Eq. 7), the superficial velocity field is updated as:

$$u(z,t) = -\left[\frac{\varepsilon_b^3 d_p^2}{150\,\mu(1-\varepsilon_b)^2}\right]\frac{\partial p}{\partial z} \tag{S7}$$

S2.2.2 Axial dispersion

We apply the widely used correlation proposed by Wakao and Kagei (1982), which provides reliable estimates for a wide range of Reynolds numbers in packed beds [2]:

$$D_{\mathrm{ax},i} = \frac{D_{m,i}}{\varepsilon_b}\,(20 + 0.5\,\mathrm{Re}\cdot\mathrm{Sc}_i) \tag{S8}$$

Here, $D_{m,i}$ is the binary molecular diffusion coefficient of species i in the gas mixture, ε_b is the bed porosity, $\mathrm{Re} = \rho v d_p/\mu$ is the particle Reynolds number, and $\mathrm{Sc}_i = \mu/(\rho D_{m,i})$ is the Schmidt number of species i.

S2.2.3 Radial dispersion

Radial dispersion is crucial in axi-symmetric-2D models to represent non-uniform radial concentration profiles. The model implemented is based on Coelho (1988), who proposed

a correlation that includes a molecular diffusion contribution and a convective dispersion term [3]:

$$D_{\mathrm{rad},i} = \frac{D_{m,i}}{\sqrt{2}} + \frac{v_{\mathrm{inlet}} \cdot d_p}{12} \tag{S9}$$

The first term accounts for diffusion across streamlines, while the second arises from flow-induced dispersion, which becomes significant at higher superficial velocities.

S2.2.4 Axial conduction

Again, we apply the correlation by Wakao and Kagei (1982):

$$\lambda_{\mathrm{ax}} = \lambda_{\mathrm{g,mix}} \left(7 + 0.5\,\mathrm{Re} \cdot \mathrm{Pr}\right) \tag{S10}$$

Here, $\lambda_{\mathrm{g,mix}}$ is the thermal conductivity of the gas mixture, and $\mathrm{Pr} = \mu c_p / \lambda_{\mathrm{g,mix}}$ is the Prandtl number.

S2.2.5 Radial conduction

Radial heat conduction in the packed bed is evaluated using a mechanistic approach (see Dixon et al. [4, 5], Heras et al.[6]), which combines a "stagnant" conductivity and the fluid flow conduction effects.

1. **Base radial Peclet number, Pe_∞.** First, the high flowrate Peclet number for heat transfer by radial fluid dispersion is calculated. For small particles, Dixon (2012) suggests that the fluid-phase radial Peclet number asymptotes to a value between 8 and 12. We select

   $$\mathrm{Pe}_\infty = 10 \quad \text{(typical mid-range value)}.$$

   In practice, one may vary it slightly (8–12) to match specific experimental data.

2. **Inverted radial Peclet term, $\mathrm{Pe}_{\mathrm{rf}}^{-1}$.** The inverse of the radial fluid Peclet number is defined as:

   $$\mathrm{Pe}_{\mathrm{rf}}^{-1} \;=\; \left(\frac{1}{\mathrm{Pe}_\infty} \;+\; \frac{\frac{2}{3}\,\varepsilon_b}{\mathrm{Re}\,\mathrm{Pr}}\right).$$

   representing an interpolation between the molecular and turbulent limits. If $v_{\mathrm{inlet}} = 0$, then the entire "flow-driven" contribution is zero, reverting to a purely stagnant scenario.

3. **Effective solid conduction coefficient, λ_{r}^0.**

   The effective solid conduction coefficient is typically estimated using the approach of Zehner and Schlünder (1978) [7], which is the most widely used and best validated correlation for fixed-bed systems [8].

   $$\frac{\lambda_{\mathrm{r}}^0}{\lambda_{\mathrm{f}}} = 1 - \sqrt{1-\varepsilon_b} + \lambda_{\mathrm{r}}^s,$$

   where:

   $$\lambda_{\mathrm{r}}^s = \frac{2\sqrt{1-\varepsilon_b}}{1 - K^{-1}\,B} \left[\frac{(1-K^{-1})\,B}{(1-K^{-1}\,B)^2}\,\ln\!\Big(\frac{1}{K^{-1}\,B}\Big) \;-\; \frac{B+1}{2} \;-\; \frac{B-1}{1-K^{-1}\,B}\right],$$

$$B = C\left(\frac{1-\varepsilon_b}{\varepsilon_b}\right)^{\frac{10}{9}}, \quad \text{and} \quad C \approx 1.25.$$

Here, $K^{-1} = \lambda_{\mathrm{g,mix}}/\lambda_p$, with $\lambda_{\mathrm{g,mix}}$ the gas-phase mixture conductivity and λ_p the particle conductivity. The exponent 10/9 reflects the empirically observed formation of conduction chains through contacting particles, originally discussed by Dixon (1979).

4. **Final effective radial conductivity, $\lambda_{\mathrm{r}}^{\mathrm{eff}}$.**

   The final effective radial thermal conductivity is then calculated using a mechanistic interpretation that accounts for both stagnant conduction and convective dispersion:

$$\frac{\lambda_{\mathrm{r}}^{\mathrm{eff}}}{\lambda_{\mathrm{g,mix}}} = \begin{cases} \frac{\lambda_{\mathrm{r}}^{0}}{\lambda_{\mathrm{g,mix}}}, & \text{if } v_{\mathrm{inlet}} = 0, \\ \frac{\lambda_{\mathrm{r}}^{0}}{\lambda_{\mathrm{g,mix}}} + \mathrm{Pe}_{\mathrm{rf}}^{-1}\,\mathrm{Pr}\,\mathrm{Re}, & \text{otherwise.} \end{cases}$$

   In the absence of flow ($v_{\mathrm{inlet}} = 0$), the system exhibits purely stagnant conduction. When flow is present, an additional term proportional to $\mathrm{Pe}_{\mathrm{rf}}^{-1}\,\mathrm{Pr}\,\mathrm{Re}$ is added to capture the contribution of convective dispersion.

S2.2.6 Heat transfer coefficients

To describe the heat exchange between the internal bed and the wall, an apparent wall heat-transfer coefficient h_w or, equivalently, a wall Nusselt number $\mathrm{Nu}_w \equiv h_w\, d_p/\lambda_{\mathrm{g,mix}}$ was defined, exploiting the so-called "h_w - λ_{r}" model.

From Yagi and Kunii (1960), a "mechanistic" formula incorporating both stagnant and convective contributions near the wall is obtained:

$$\mathrm{Nu}_w \;=\; \mathrm{Nu}_{w0} \;+\; \left(\frac{1}{\mathrm{Nu}_w^{*}} \;+\; \frac{1}{\mathrm{Nu}_m}\right)^{-1} \tag{S11}$$

where Nu_{w0} accounts for the contribution of solid-phase conduction, Nu_w represents the true fluid-wall film heat transfer coefficient, and Nu_w^{*} captures the effect of lateral convective heat transfer in the near-wall region.

The individual contributions can be obtained using:

- $$\mathrm{Nu}_{w0} = \left(1.3 + \frac{5}{N}\right)\left(\frac{\lambda_{\mathrm{r}}^{0}}{\lambda_{\mathrm{f}}}\right) \quad \text{(Martin and Nilles, 1960)}$$
- $$\mathrm{Nu}_w^{*} = 0.3\,\mathrm{Pr}^{1/3}\,\mathrm{Re}^{0.75} \quad \text{(Dixon, 2012)}$$
- $$\mathrm{Nu}_m = 0.054\,\mathrm{Pr}\,\mathrm{Re} \quad \text{(Yagi and Kunii, 1960)}$$

Once Nu_w is obtained, the (dimensional) wall heat-transfer coefficient can be calculated:

$$h_w \;=\; \frac{\mathrm{Nu}_w\,\lambda_{\mathrm{g,mix}}}{d_p}. \tag{S12}$$

Finally, many pseudo-1D reactor models adopt an *overall* 1D internal heat-transfer coefficient U_w (or simply U), relating the tube wall to the bed-average temperature via a single lumped resistance [5]. Dixon (1996) showed that a better formula for U than the classic "two-resistance-in-series" approach is:

$$U_w \;=\; \left(\frac{1}{h_w} \;+\; \frac{d_b}{6\,\lambda_{\mathrm{rad}}}\,\frac{\mathrm{Bi}+3}{\mathrm{Bi}+4}\right)^{-1}, \tag{S13}$$

where

$$\mathrm{Bi} \;=\; \frac{(h_w)\,\frac{d_b}{2}}{\lambda_{\mathrm{rad}}}$$

is the bed Biot number. This enhanced formula captures the shifting balance between wall convection (h_w) and radial conduction (λ_{rad}). Comparisons of 1D, 2D, and two-phase continuum models by Dixon et al. show that this approach greatly reduces errors in predicting axial temperature profiles and hot-spot conditions, especially in systems where radial conduction and near-wall phenomena strongly affect reactor performance.

S2.2.7 Physical parameters

Mixture density $\rho_{\mathrm{g,mix}}$: The density is computed using the ideal gas law.

$$\rho_{\mathrm{g,mix}} = \sum_i c_i M_i$$

Mixture viscosity $\mu_{\mathrm{g,mix}}$: The mixture viscosity is estimated using Wilke's rule. Pure component viscosities are first calculated using the Chapman–Enskog theory:

$$\mu_i = \frac{1.109 \times 10^{-6}\sqrt{T}}{\Omega_{ij}}$$

where Ω_{ij} is the collision integral computed via the Neufeld correlation. Then, the Wilke mixture rule is applied:

$$\mu_{\mathrm{g,mix}} = \sum_i \frac{y_i \mu_i}{\sum_j y_j \phi_{ij}}$$

with the interaction term ϕ_{ij} calculated from molar masses and viscosities [9].

Mixture heat capacities $c_{p,\mathrm{g}}$ and $c_{v,\mathrm{g}}$: The molar heat capacity at constant pressure is calculated using the Shomate equation:

$$c_{p,i} = A + Bt + Ct^2 + Dt^3 + \frac{E}{t^2} \quad \text{with } t = \frac{T}{1000}$$

Values for A–E are taken from the NIST database [10].

Mixture thermal conductivity $\lambda_{\mathrm{g,mix}}$: The mixture thermal conductivity is evaluated using mole-fraction weighted averaging of the pure components:

$$\lambda_{\mathrm{g,mix}} = \sum_i y_i \lambda_i$$

Solid heat capacity $c_{p,\text{solid}}$: The specific heat capacity of Lewatit® is fitted to a temperature-dependent model given by Low et al. [11]:

$$c_{p,\text{solid}} = \frac{a}{T^2} + bT - c$$

Molecular and effective diffusion coefficients D_{ij}, $D_{m,i}$: The binary diffusion coefficients are calculated using the Fuller–Schettler–Giddings model [12]:

$$D_{ij} = \frac{0.001 T^{1.75} \sqrt{\frac{1}{M_i} + \frac{1}{M_j}}}{\left(\frac{P}{101325}\right) \left(V_i^{1/3} + V_j^{1/3}\right)^2}$$

where V_i is the diffusion volume of species i.

Finally, in ternary mixtures with one species in excess, the Wilke-like approximation is used to obtain the mixture diffusion coefficient of component i [13]:

$$D_{m,i} = \frac{1 - y_i}{\sum_{j \neq i} \frac{y_j}{D_{ij}}}$$

S2.3 Initial and Boundary conditions

The boundary conditions for each step of the TVSA cycle are summarized below. The column length is L, with the inlet at $z = 0$ and the outlet at $z = L$. The initial conditions are applied only to the startup step, assuming an empty bed filled with N_2 and O_2 at ambient temperature and pressure.

Table S2: Boundary conditions of the adsorption step.

State	Inlet ($z = 0$)	Outlet ($z = L$)
Composition (y_i)	$v\, y_i - D_{\text{ax},i} \dfrac{\partial y_i}{\partial z} = v^{\text{feed}}\, y_i^{\text{feed}}$	$\dfrac{\partial y_i}{\partial z} = 0$
Pressure/velocity	$v = v^{\text{feed}}$	$p = p_{amb}$
Bed temperature (T)	$v\, T - \lambda_{\text{ax}} \dfrac{\partial T}{\partial z} = v^{\text{feed}}\, T^{\text{feed}}$	$\dfrac{\partial T}{\partial z} = 0$
Wall temperature (T_{wall})	$T_{wall} = T_{jacket}$	$T_{wall} = T_{jacket}$

Table S3: Boundary conditions of the vacuum step

State	Inlet ($z = 0$)	Outlet ($z = L$)
Composition (y_i)	$\dfrac{\partial y_i}{\partial z} = 0$	$\dfrac{\partial y_i}{\partial z} = 0$
Pressure/velocity	$v = 0$	$\dfrac{\partial p}{\partial z} = \alpha_{\text{blow}}(p_{\text{vac}} - p)$
Bed temperature T	$\dfrac{\partial T}{\partial z} = 0$	$\dfrac{\partial T}{\partial z} = 0$
Wall temperature T_{wall}	$T_{wall} = T_{jacket}$	$T_{wall} = T_{jacket}$

Table S4: Boundary conditions of the pre-heating/wall-heated desorption step

State	Inlet ($z = 0$)	Outlet ($z = L$)
Composition (y_i)	$\dfrac{\partial y_i}{\partial z} = 0$	$\dfrac{\partial y_i}{\partial z} = 0$
Pressure/velocity	$v = 0$	$p = p_{\text{vac}}$
Bed temperature T	$\dfrac{\partial T}{\partial z} = 0$	$\dfrac{\partial T}{\partial z} = 0$
Wall temperature T_w	$T_w = T_H$	$T_w = T_H$

Table S5: Boundary conditions of the steam-assisted desorption step.

State	Inlet ($z = 0$)	Outlet ($z = L$)
Composition ($y_{\text{H}_2\text{O}}$)	$v\, y_{\text{H}_2\text{O}} - D_{\text{ax,H}_2\text{O}} \dfrac{\partial y_{\text{H}_2\text{O}}}{\partial z} = v_{\text{steam}}^{\text{feed}}\, y_{\text{H}_2\text{O}}^{\text{feed}}$	$\dfrac{\partial y_{\text{H}_2\text{O}}}{\partial z} = 0$
Pressure/velocity	$v = v_{\text{steam}}^{\text{feed}}$	$p = p_{\text{vac}}$
Bed temperature (T)	$v\, T - \lambda_{\text{ax}} \dfrac{\partial T}{\partial z} = v_{\text{steam}}^{\text{feed}}\, T_{\text{steam}}^{\text{feed}}$	$\dfrac{\partial T}{\partial z} = 0$
Wall temperature (T_{wall})	$T_{wall} = T_{jacket}$	$T_{wall} = T_{jacket}$

Table S6: Boundary conditions of the pressurization step.

State	Inlet ($z = 0$)	Outlet ($z = L$)
Composition (y_i)	$v\, y_i - D_{\text{ax}} \dfrac{\partial y_i}{\partial z} = v^{\text{feed}}\, y_i^{\text{feed}}$	$\dfrac{\partial y_i}{\partial z} = 0$
Pressure/velocity	$\dfrac{\partial p}{\partial z} = \alpha_{\text{press}}\,(p^{\text{feed}} - p)$	$v = 0$
Bed temperature (T)	$v\, T - \lambda_{\text{ax}} \dfrac{\partial T}{\partial z} = v^{\text{feed}}\, T^{\text{feed}}$	$\dfrac{\partial T}{\partial z} = 0$
Wall temperature (T_{wall})	$T_{wall} = T_{jacket}$	$T_{wall} = T_{jacket}$

S2.4 Model validation

S2.4.1 Young et al. simulated data

The model was validated against outlet CSS profiles reported by Young et al. [1] and showed excellent agreement. To enable a direct comparison, the model from the main text was extended with the additional cooling step included in Young's work. The outlet profiles refer to the cyclic steady state (CSS), reached after two cycles, as reported in the figures title.

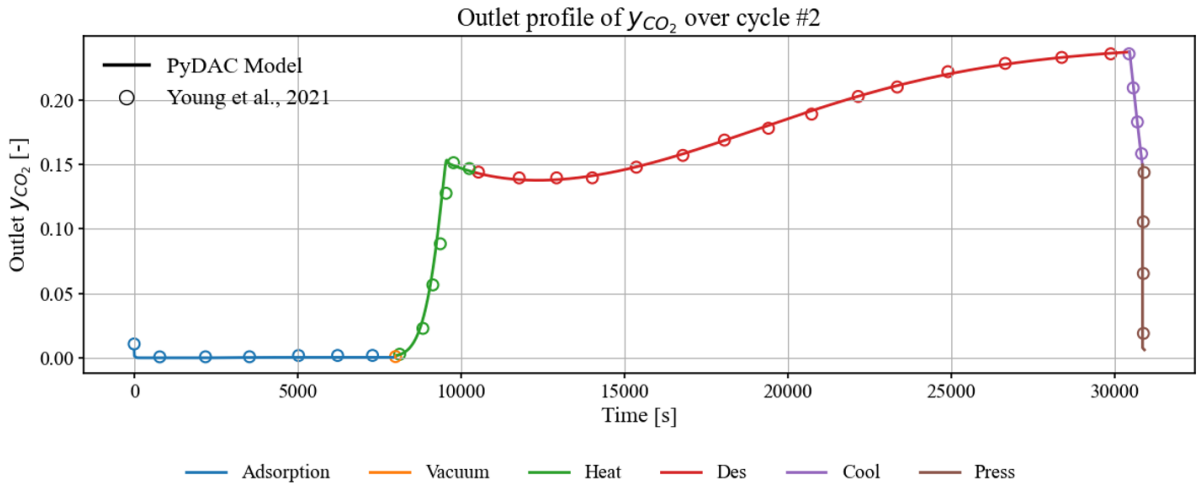

Figure S9: Composition outlet profiles validation.

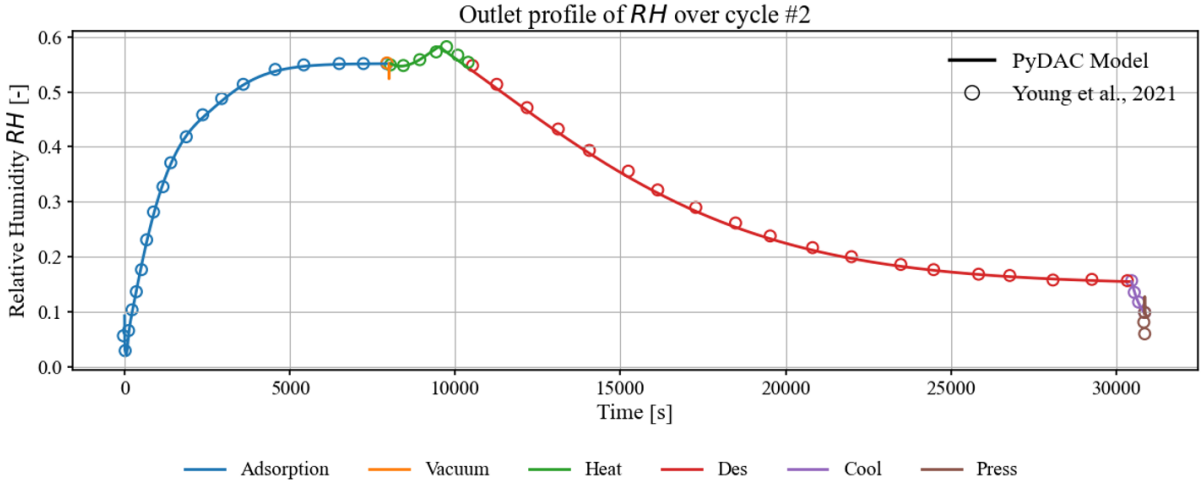

Figure S10: Relative humidity outlet profiles validation.

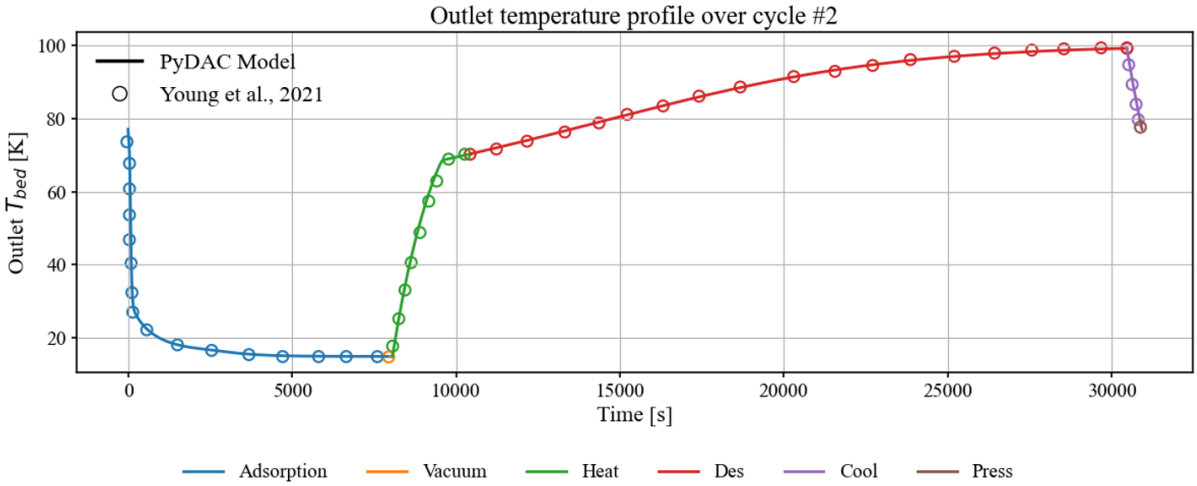

Figure S11: Bed temperature outlet profile validation.

S2.4.2 Petersen et al. experimental data

We have performed an independent comparison against experimental dynamic column breakthrough data reported by Petersen et al. for Lewatit® VPOC 1065 [14]. In this comparison, the present model was run using the exact operating conditions, inlet compositions, and temperature boundaries reported in the experimental study, allowing for a direct assessment of model fidelity.

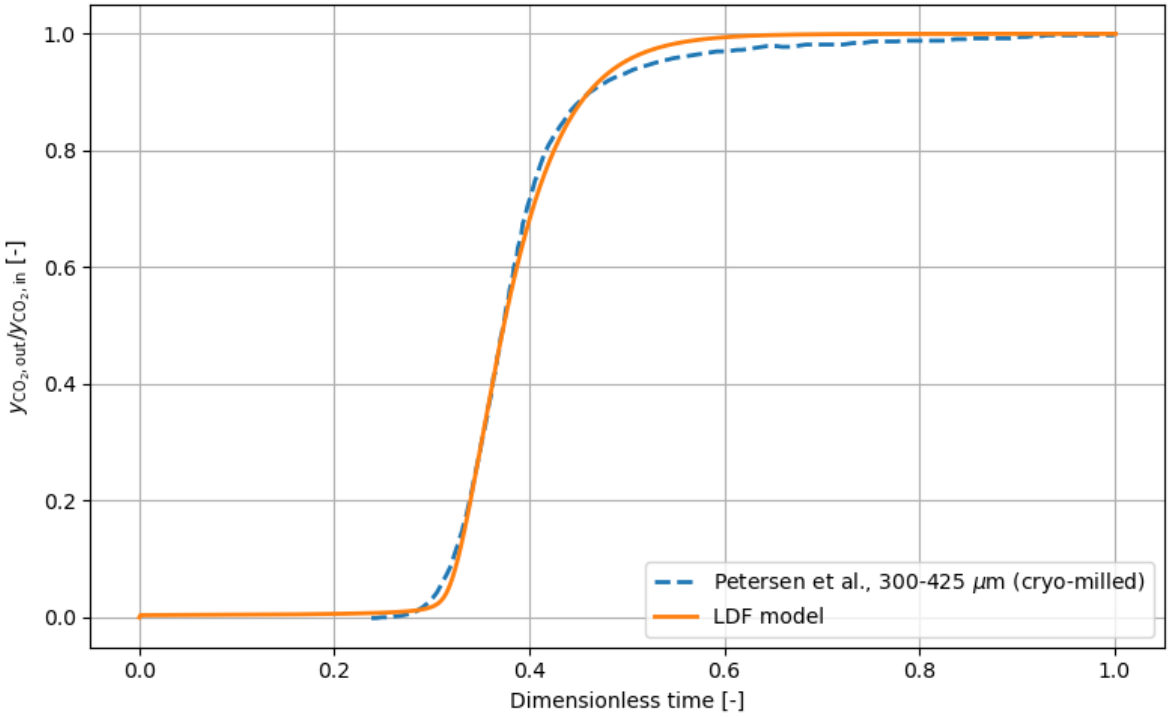

Figure S12: Validation of the dynamic breakthrough behavior against experimental data from Petersen et al. (cryo-milled, particle size 300-425 μm). The normalized outlet CO_2 mole fraction ($y_{CO_2,out}/y_{CO_2,in}$) is shown as a function of dimensionless time.

Overall, the model reproduces the main features of the measured transient response,

including the characteristic front propagation, the breakthrough time, and the approach to saturation. Minor deviations are observed around the steepest part of the profile, which can reasonably be attributed to the intrinsic limitations of a lumped kinetic representation (LDF) and to uncertainties in transport closures under the specific experimental conditions.

It is also worth noting that the fitted LDF mass-transfer coefficient obtained from Petersen et al. breakthrough data ($k_{\mathrm{LDF}} = 2 \times 10^{-3}$ s^{-1}) is remarkably close to the value adopted in the main text based on Young et al. ($k_{\mathrm{LDF}} = 3 \times 10^{-3}$ s^{-1}). Although these validations involve substantially different column geometries and operating conditions, the consistency in the estimated kinetic parameter supports the robustness of the adopted LDF formulation and suggests that the model is not overly sensitive to case-specific tuning of k_{LDF} within the investigated range.

Given that the scope of this work is cycle-level performance assessment and multi-objective optimization, the LDF kinetic formulation provides an appropriate balance between physical fidelity and numerical efficiency. The implementation of more detailed kinetic frameworks (e.g., pore diffusion or multi-resistance models) is expected to further refine the prediction of the breakthrough front shape and will be considered in future developments.

S2.5 Model setup and reference case

Table S7: Reference case parameters, geometry, particle properties and solver settings used in the packed-bed simulations

Category	Parameter	Value
Reference conditions (adsorption step)		
Temperature	T_{ref}	298.15 K
Pressure	p_{ref}	101325 Pa
Relative humidity	$\mathrm{RH}_{\mathrm{ref}}$	0.5
Inlet mole fraction CO_2	$y_{\mathrm{CO_2,ref}}$	400 ppm
Superficial velocity	$v_{\mathrm{sup,ref}}$	0.5 m s^{-1}
Geometry and particle properties		
Bed length	L_b	0.0181 m [15]
Bed radius	R_b	0.145 m [15]
Wall thickness	t_b	0.017 m [15]
Bed porosity	ε_b	0.37 [15]
Particle density	ρ_p	880 kg m^{-3} [1]
Particle radius	R_p	0.25 mm [1]
Spatial discretization and solver settings		
Axial grid points	N_z	100
Relative tolerance	rtol	10^{-6}
Absolute tolerance	atol	10^{-8}

Table S8: Kinetic, transport and thermophysical parameters used in the packed-bed simulations

Category	Parameter	Value
Kinetics and flow coefficients		
LDF mass transfer coefficient (CO_2)	$k_{\mathrm{LDF,CO2}}$	0.003 s^{-1} [1]
LDF mass transfer coefficient (H_2O)	$k_{\mathrm{LDF,H2O}}$	0.0086 s^{-1} [1]
Blowdown parameter	α_{blow}	0.01
Pressurisation parameter	α_{press}	0.01
Thermal properties		
Particle thermal conductivity	λ_p	0.43 W m^{-1} K^{-1} [16]
Wall heat capacity	$c_{p,w}$	513 J kg^{-1} K^{-1} [15]
Wall density	ρ_w	7800 kg m^{-3} [15]
External heat transfer coefficient	h_{ext}	26 W m^{-2} K^{-1} [15]
Wall thermal conductivity	λ_w	16 W m^{-1} K^{-1} [15]
Adsorption thermodynamics		
Heat of adsorption (CO_2)	$\Delta H_{ads,\mathrm{CO_2}}$	−70,000 J mol^{-1} [1]
Heat of adsorption (H_2O)	$\Delta H_{ads,\mathrm{H_2O}}$	−46,000 J mol^{-1} [1]
Dry air O_2/N_2 ratio	$y_{\mathrm{O_2}}/y_{\mathrm{N_2}}$	3.73 [17]

The parameters α_{blow} and α_{press} were set such that the blowdown and pressurization steps last about 60 s. Although in real systems these steps occur over several minutes, the impact of this simplification is minimal given that the adsorption, pre-heating, and desorption steps operate on timescales of several hours.

S2.6 Energy consumption estimation

The model tracks the instantaneous energy consumption of each auxiliary unit operation (compressor, vacuum pump, blower/fan, and thermal jacket) at each integration time step. Each power contribution is integrated in time within the ODE system to give the total energy consumption per cycle.

S2.6.1 Air-moving device selection (fan vs blower vs compressor)

Depending on the severity of the pressure drop, the appropriate correlation is selected:

$$\overline{\Delta p} \equiv \overline{p_{\text{in}} - p_{\text{out}}}$$

Specifically, we use the following heuristic thresholds:

$$P_{\text{am}}(\overline{\Delta p}) = \begin{cases} P_{\text{fan}} & \text{if } \overline{\Delta p} \leq 10 \text{ kPa} \\ P_{\text{blow}} & \text{if } 10 \text{ kPa} < \overline{\Delta p} \leq 200 \text{ kPa} \\ P_{\text{comp}} & \text{if } \overline{\Delta p} > 200 \text{ kPa} \end{cases}$$

where P_{fan}, P_{blow}, and P_{comp} are given by:

$$P_{\text{fan}} = \frac{1}{\eta_{\text{fan}}} \Delta p \, Q_{\text{in}} \tag{S14}$$

$$P_{\text{blow}} = \frac{1}{\eta_{\text{blow}}} p_{\text{in}} Q_{\text{in}} \ln\left(\frac{p_{\text{in}}}{p_{\text{out}}}\right) \tag{S15}$$

$$P_{\text{comp}} = \frac{1}{\eta_{\text{comp}}} \frac{\gamma}{\gamma - 1} p_{\text{in}} Q_{\text{in}} \left[\left(\frac{p_{\text{in}}}{p_{\text{out}}}\right)^{\frac{\gamma-1}{\gamma}} - 1\right] \tag{S16}$$

where $\Delta p = p_{\text{in}} - p_{\text{out}}$, p_{in} and p_{out} are inlet and outlet pressures, Q_{in} is the volumetric flow rate, $\gamma = c_p/c_v$ is the heat capacity ratio of the mixture, and η_{i} is the assumed efficiency (0.7 when vendor data are unavailable).

S2.6.2 Vacuum pump energy

The vacuum pump power is evaluated using a fully compressible polytropic model with pressure-dependent efficiency η_{vac} fitted to the correlation of Ward et al.:

$$\eta_{\text{vac}} = \frac{0.8 \times 19.55 \, (p_{\text{out}}/10^5)}{1 + 19.55 \, (p_{\text{out}}/10^5)} \tag{S17}$$

$$P_{\text{vac}} = \frac{1}{\eta_{\text{vac}}} \frac{\gamma}{\gamma - 1} p_{\text{out}} Q_{\text{out}} \left[\left(\frac{p_{\text{amb}}}{p_{\text{out}}}\right)^{\frac{\gamma-1}{\gamma}} - 1\right] \tag{S18}$$

with p_{amb} the ambient pressure.

S2.6.3 Jacket thermal energy

The instantaneous thermal duty exchanged with the wall is obtained from the local wall–bed temperature difference:

$$q_{\mathrm{wall}}(z) = h_{\mathrm{int}}\,(T_{\mathrm{wall}}(z) - T(z)) \tag{S19}$$

and integrated along the axial coordinate to obtain the instantaneous jacket power:

$$P_{\mathrm{jacket}} = \int_0^{L_b} q_{\mathrm{wall}}(z)\, 2\pi R_b\, dz \tag{S20}$$

where h_{int} is the internal wall–fluid heat transfer coefficient, R_b the bed radius, T_{wall} the wall temperature profile and T the bed temperature.

S2.7 Thermodynamic Calculations

S2.7.1 Steam energy

The energy required for steam injection is estimated as the sum of three contributions: (i) sensible heating of liquid water from the feed temperature to the boiling temperature at the column pressure, (ii) phase change at T_{bp}, and (iii) superheating of the resulting steam up to the injection reference temperature.

The steam mass consumed over a desorption step of duration Δt is

$$m_s \;=\; \dot{m}_s\,\Delta t,$$

where $\dot{m}_s$ is the constant steam mass flow rate.

The saturation temperature at feed pressure p_{feed} and the latent heat of vaporization are correlated as (Ward *et al.*)

$$T_{\mathrm{bp}}(p_{\mathrm{feed}}) \;=\; 197\left(\frac{p_{\mathrm{feed}}}{10^5}\right)^{0.1367} - 97.97 + 273.15 \quad [\mathrm{K}],$$

$$h_{\mathrm{bp}}(p_{\mathrm{feed}}) \;=\; -446.2\left(\frac{p_{\mathrm{feed}}}{10^5}\right)^{0.1508} + 2707 \quad [\mathrm{kJ\,kg^{-1}}].$$

The three enthalpy contributions per unit mass are:

$$\Delta h_{\mathrm{heat}} \;=\; c_{p,l}\,\big(T_{\mathrm{bp}} - T_{\mathrm{ref}}\big),$$

$$\Delta h_{\mathrm{bp}} \;=\; h_{\mathrm{bp}}(p_{\mathrm{feed}}),$$

$$\Delta h_{\mathrm{sup}} \;=\; \frac{a}{3}\big(T_{\mathrm{feed}}^3 - T_{\mathrm{bp}}^3\big) + \frac{b}{2}\big(T_{\mathrm{feed}}^2 - T_{\mathrm{bp}}^2\big) + c(T_{\mathrm{feed}} - T_{\mathrm{bp}})\,,$$

with $c_{p,l} = 4.186\ \mathrm{kJ\,kg^{-1}\,K^{-1}}$ and steam heat capacity correlation $c_{p,g}(T) = aT^2 + bT + c$ with $a = 1.012 \times 10^{-6}$, $b = -3.594 \times 10^{-4}$, $c = 1.882$ (kJ kg^{-1} K^{-1}).

The total steam energy is then

$$Q_{\mathrm{steam}} \;=\; m_s\,\Big(\,\Delta h_{\mathrm{heat}} + \Delta h_{\mathrm{vap}} + \Delta h_{\mathrm{sup}}\,\Big),$$

S2.7.2 Condenser duty

The condenser heat load is evaluated as the difference between inlet and outlet enthalpies, following the enthalpy balance around the unit. We define reference enthalpies as ideal gases at $T_{ref} = T_{\mathrm{cond}}$. Therefore, the instantaneous duty is

$$\dot{Q}_{\mathrm{cond}}(t) \;=\; H_{\mathrm{feed}}(t) \;-\; H_v(t) \;-\; H_\ell(t) \quad [\mathrm{W}],$$

and the cumulative condenser energy is obtained by time integration. The terms are a function of time since the condenser feed is the outlet stream from the desorption step.

Feed enthalpy The feed is entirely in the gas phase. Its enthalpy relative to the reference is given by the sensible heating from the reference temperature (T_{cond}) to T_{feed}:

$$H_{\mathrm{feed}}(t) \;=\; \dot{n}_{\mathrm{feed}}(t) \sum_i z_i(t)\, c_{p,i}^{g} \left(T_{\mathrm{feed}}(t) - T_{\mathrm{cond}}\right).$$

Vapor outlet enthalpy With the chosen reference, the vapor outlet (non-condensables at T_{cond}) has zero enthalpy contribution:

$$H_v(t) \;=\; 0.$$

Condensate enthalpy The condensate enthalpy is evaluated component-wise, by constructing a thermodynamic path from the vapor reference state (ideal gas at T_{cond}) to the liquid state at T_{cond} and then adding the enthalpy of mixing, with an additional mixing term to account for CO_2 dissolution into water.

For each condensable component i, the pure-component contribution is written as

$$h_{i,\ell}^{(\text{pure path})}(T_{\mathrm{cond}}) = c_{p,i}^{g} \left(T_{\mathrm{bp},i} - T_{\mathrm{cond}}\right) - \Delta H_{\mathrm{vap},i} + c_{p,i}^{\ell} \left(T_{\mathrm{cond}} - T_{\mathrm{bp},i}\right),$$

where $T_{\mathrm{bp},i}(p_{\mathrm{cond}})$ is the boiling point temperature of component i at the condenser pressure, which is equal to the chosen vacuum pressure of the desorption step.

For H_2O, this term accounts for heating of the vapor from reference temperature to $T_{\mathrm{bp,H2O}}$, condensation, and subcooling again to T_{cond}. For CO_2, since it does not form a pure liquid at p_{cond}, we include explicitly the enthalpy of dissolution into water, $\Delta\bar{h}_{\mathrm{sol,CO2}}(T_{\mathrm{cond}}, x)$.

The total condensate enthalpy is therefore

$$H_\ell(t) \;=\; \dot{n}_\ell(t) \left[x_{\mathrm{H_2O}}(t)\, h_{\mathrm{H_2O},\ell}^{(\text{pure path})}(T_{\mathrm{cond}}) + x_{\mathrm{CO_2}}(t) \left(\Delta\bar{h}_{\mathrm{sol,CO2}}(T_{\mathrm{cond}}, x) \right) \right].$$

Total condenser duty and energy The net condenser duty is then

$$\dot{Q}_{\mathrm{cond}}(t) \;=\; H_{\mathrm{feed}}(t) \;-\; H_\ell(t),$$

and the condenser energy over the step is

$$E_{\mathrm{cond}} \;=\; \int_{t_0}^{t_e nd} \dot{Q}_{\mathrm{cond}}(t)\, dt$$

The equations for the H_2O boiling point and vaporization enthalpy were provided in the steam duty calculation section. The molar enthalpy of dissolution of CO_2 in water at low pressures is calculated with the correlation of Carroll et al. (1991) [18]:

$$\Delta\bar{h}_{\mathrm{sol,CO_2}}(T) = \left(106.56 - \frac{6.2634\times10^4}{T} + \frac{7.475\times10^6}{T^2}\right)\times10^3 \quad [\mathrm{J\ mol^{-1}}],$$

where T is the absolute temperature in kelvin.

S3 Literature benchmark

S3.1 Optimized decision variables boxplot distributions

The boxplots summarize the distributions of the optimized decision variables for the (i) wall-heated and (ii) steam-assisted configurations at the reference geometry. Each variable x is normalized to its search bounds $[x_{\min}, x_{\max}]$ via

$$x^* = \frac{x - x_{\min}}{x_{\max} - x_{\min}},$$

so that $x^* = 0$ corresponds to the lower bound and $x^* = 1$ to the upper bound. The box shows the interquartile range (IQR), the horizontal line marks the median, whiskers extend to 1.5× IQR, and dots indicate outliers.

S3.1.1 Complete wall-heated and steam-assisted cases

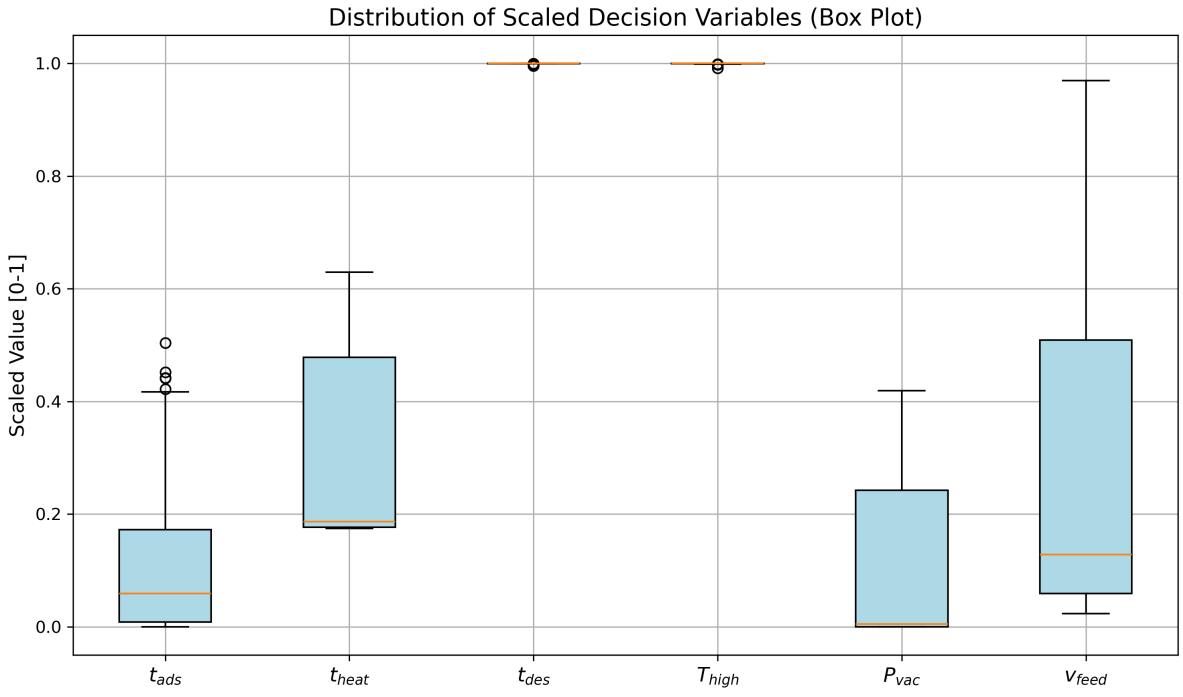

Figure S13: Wall-heated configuration optimized decision variables boxplots

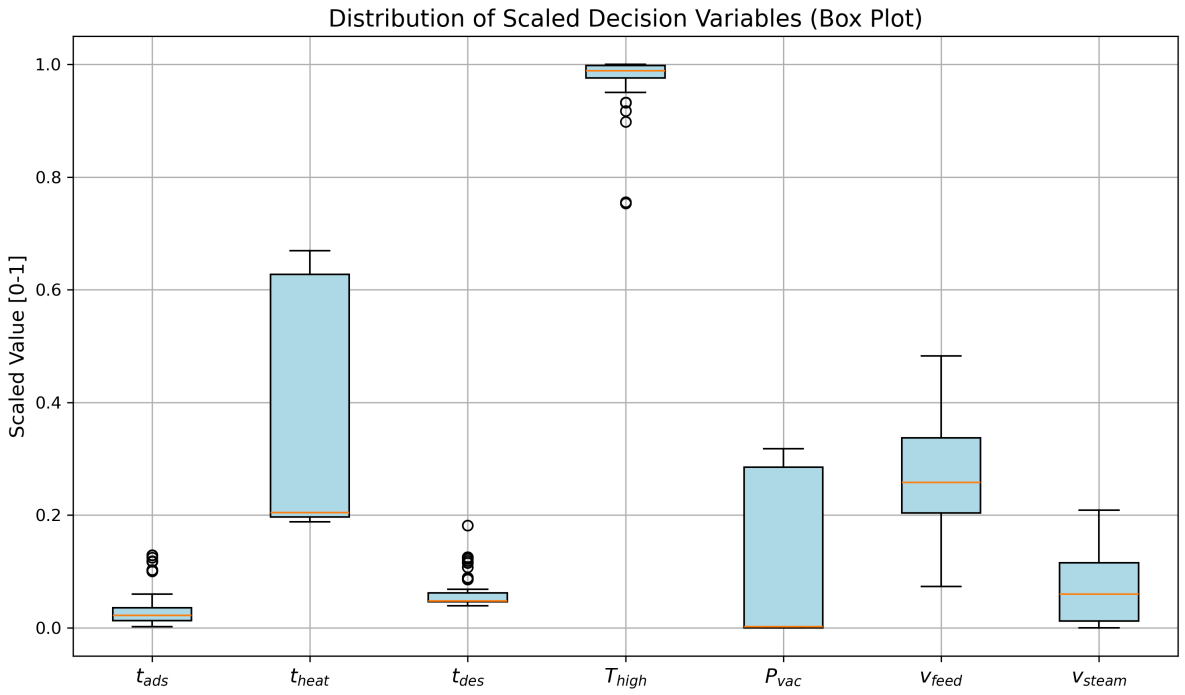

Figure S14: Steam-assisted configuration optimized decision variables boxplots.

Under the reference aspect ratio ($H_{bed}/D_{bed} = 1/16$), the wall-heated thermal bottleneck requires extended desorption periods to supply sufficient heat, which explains why the optimized desorption time t_{des} consistently saturates at its upper bound. The resulting steep rise in equivalent work with increasing productivity directly reflects this limitation. In contrast, for the steam-assisted case, the distribution of desorption times t_{des} collapses near the lower bound of the search range, confirming that desorption can be completed much more rapidly.

S3.1.2 Incomplete (No O_2, no Q_{cond}) steam-assisted case

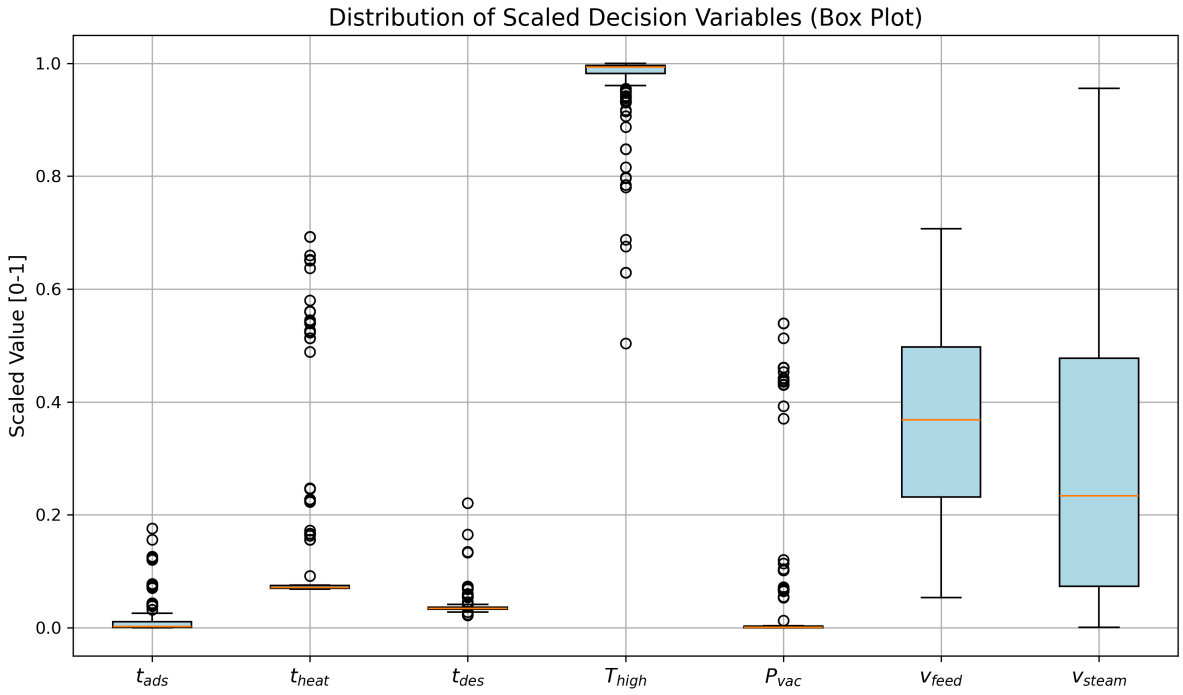

Figure S15: Steam-assisted configuration boxplots for the incomplete case where the O_2 content constraint and the condenser thermal duty were excluded.

S3.1.3 Effect of Oxygen constraint, wall-heated and steam-assisted case

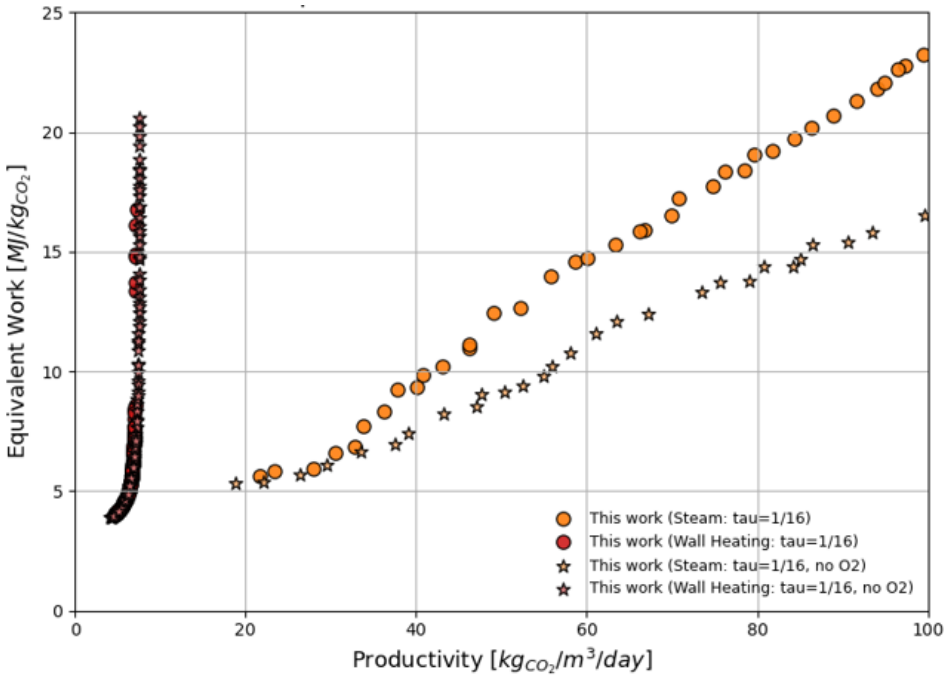

Figure S16: Effect of enforcing the O_2 purity constraint on the optimized Pareto fronts for $\tau = 1/16$, for both wall-heated and steam-assisted configurations.

S4 Aspect ratio analysis

S4.1 Step durations for wall-heated configuration

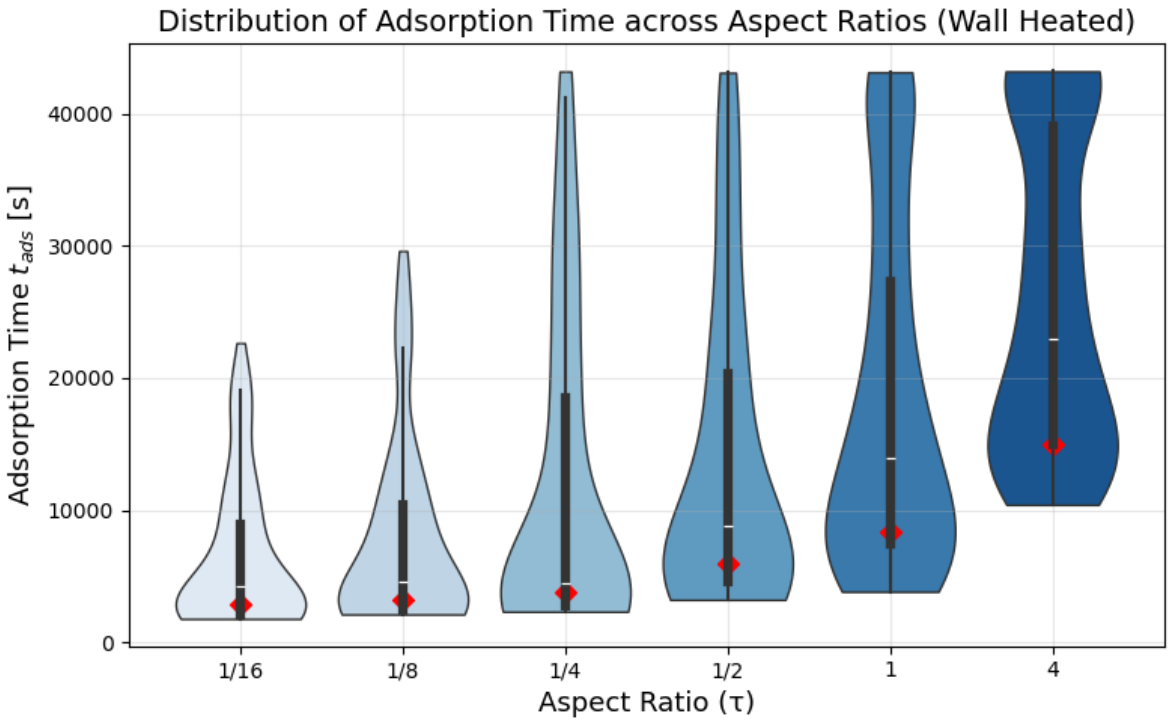

Figure S17: Wall-heated adsorption-time distribution.

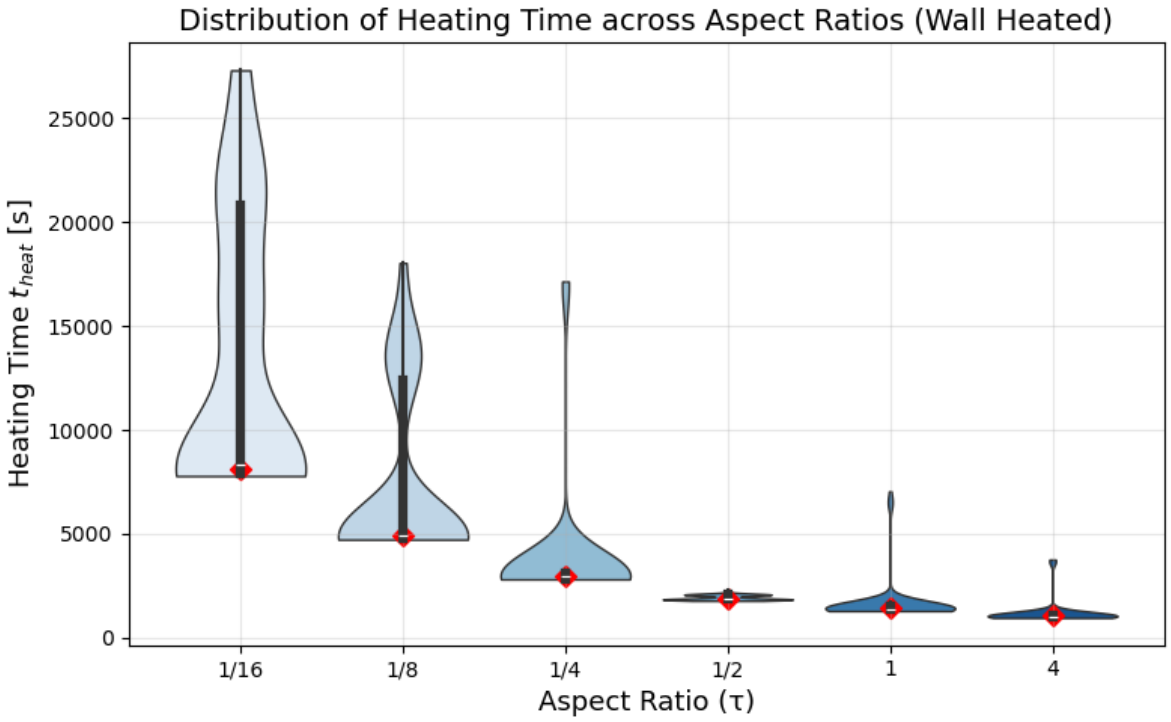

Figure S18: Wall-heated pre-heating-time distribution.

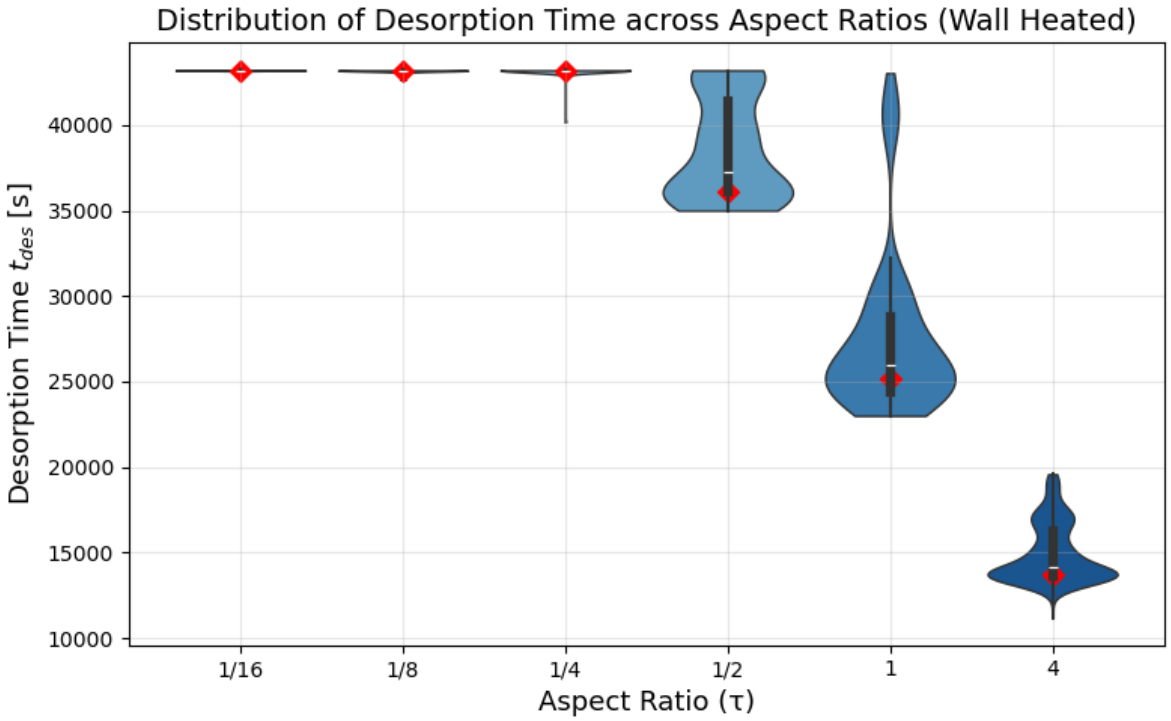

Figure S19: Wall-heated desorption-time distribution.

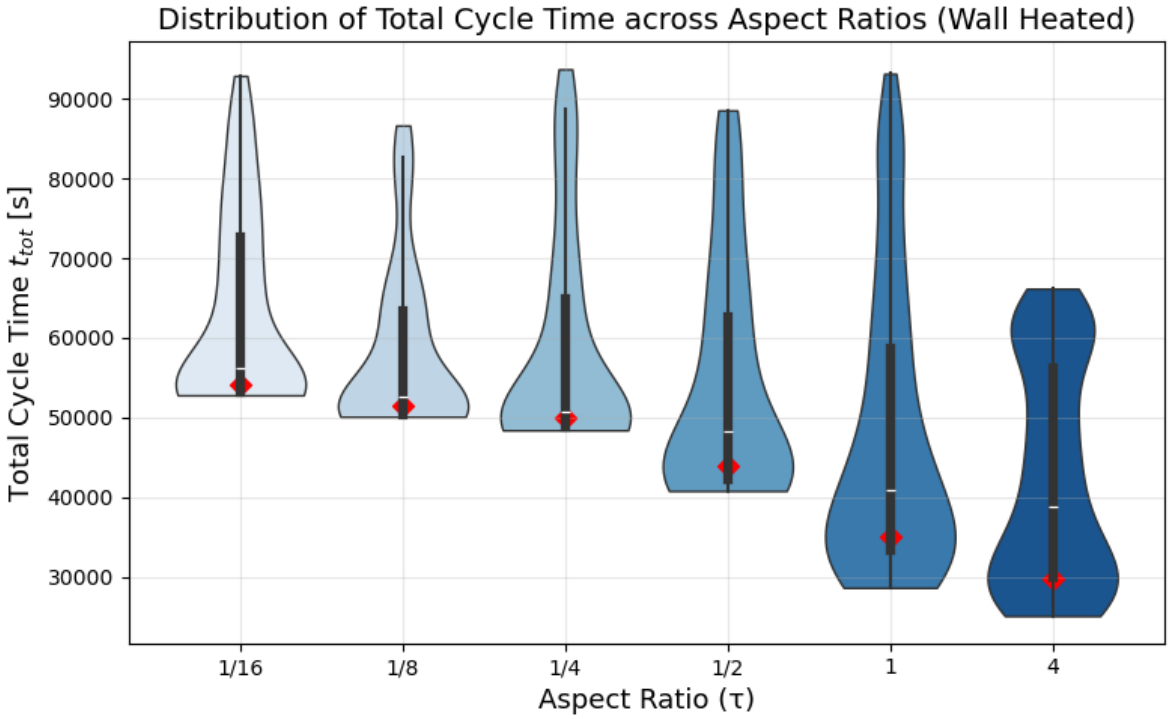

Figure S20: Wall-heated total cycle time distribution.

S4.2 Energy contributions for wall-heated configurations

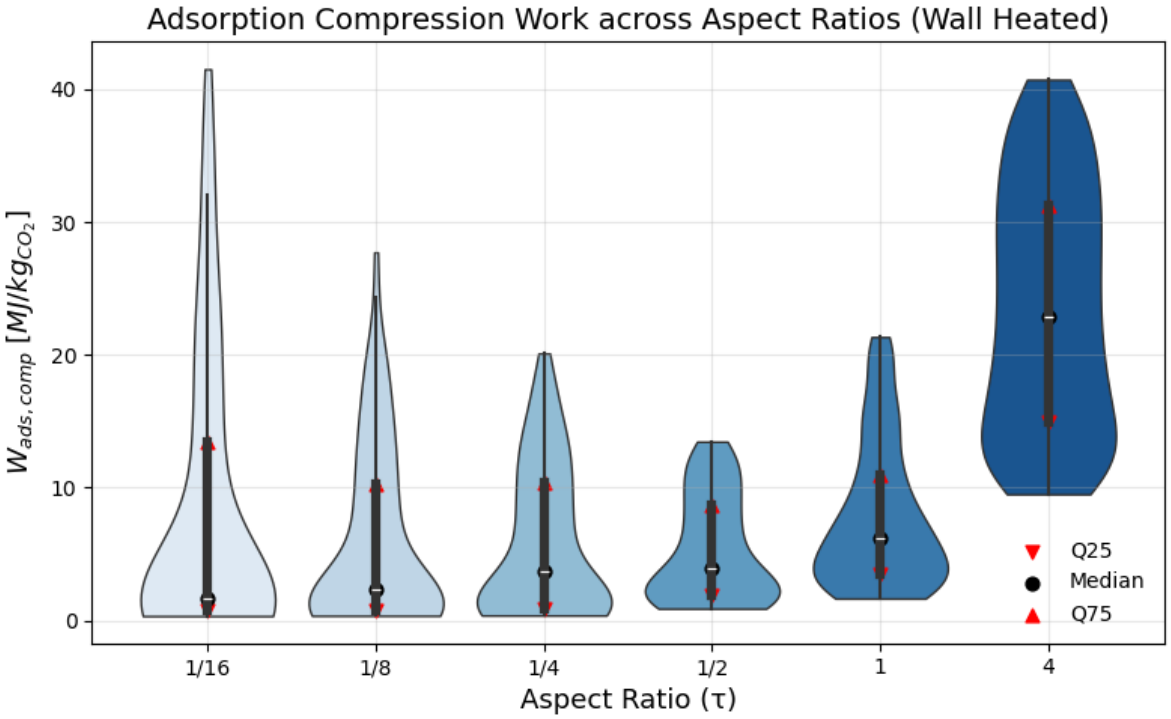

Figure S21: Wall-heated compression energy distribution.

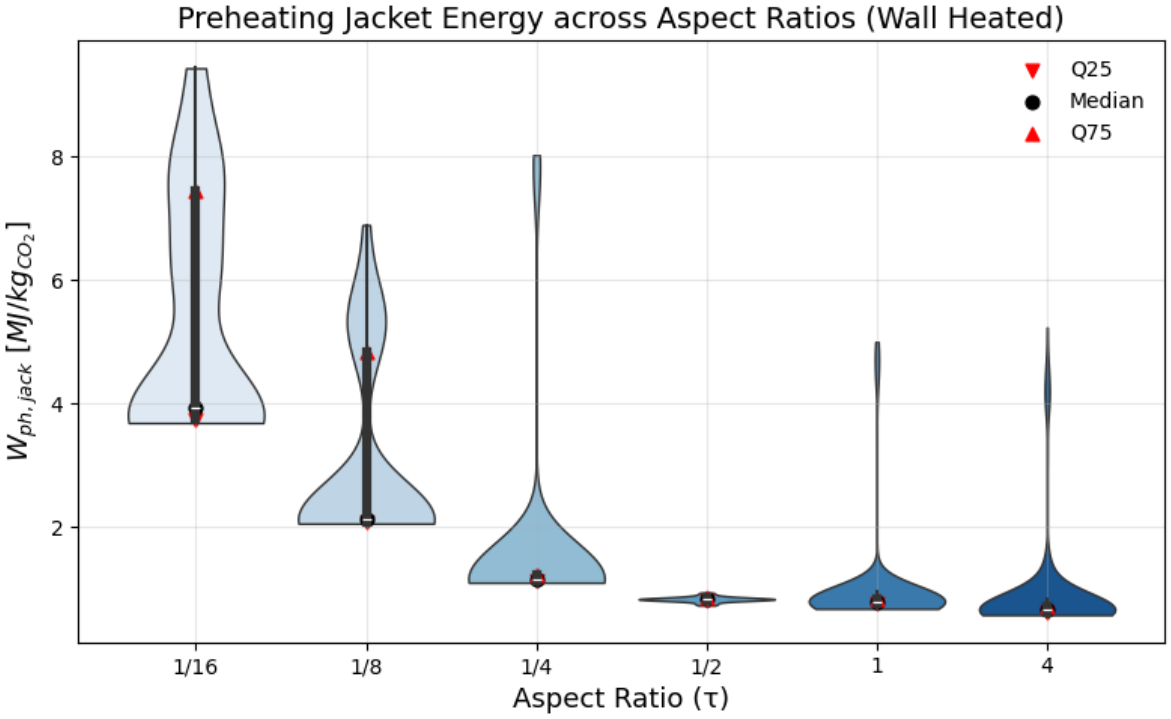

Figure S22: Wall-heated heated-jacket energy distribution for the pre-heating step.

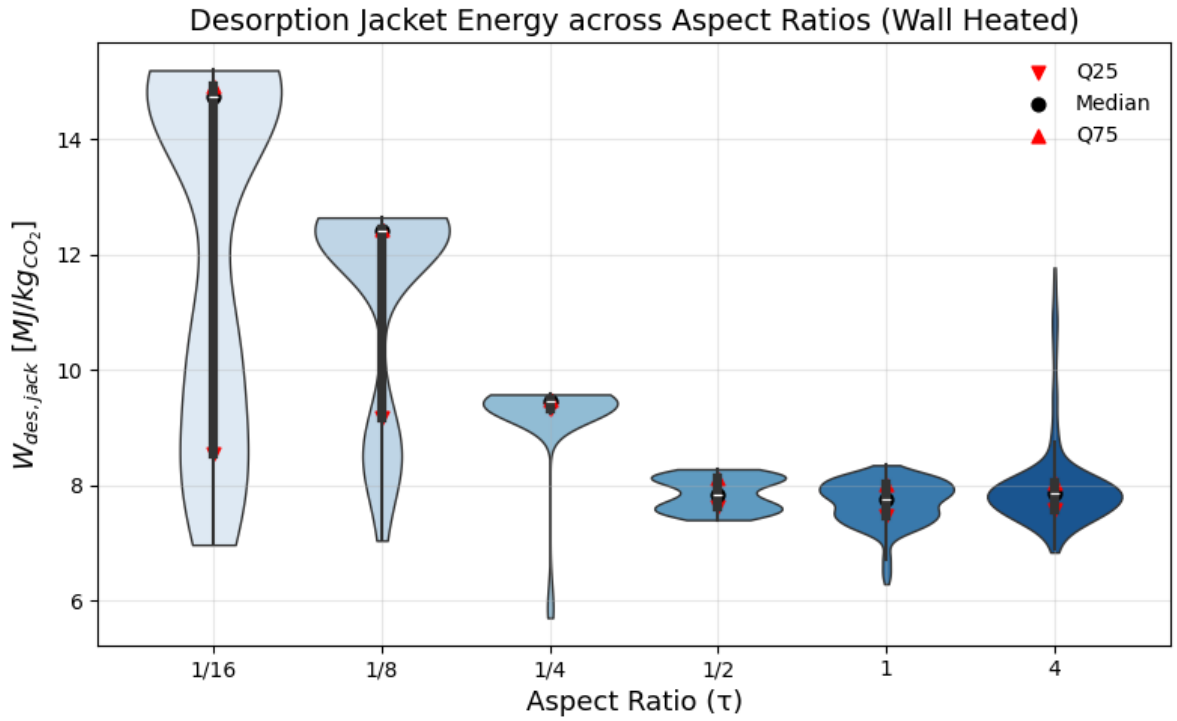

Figure S23: Wall-heated heated-jacket energy distribution for the desorption step.

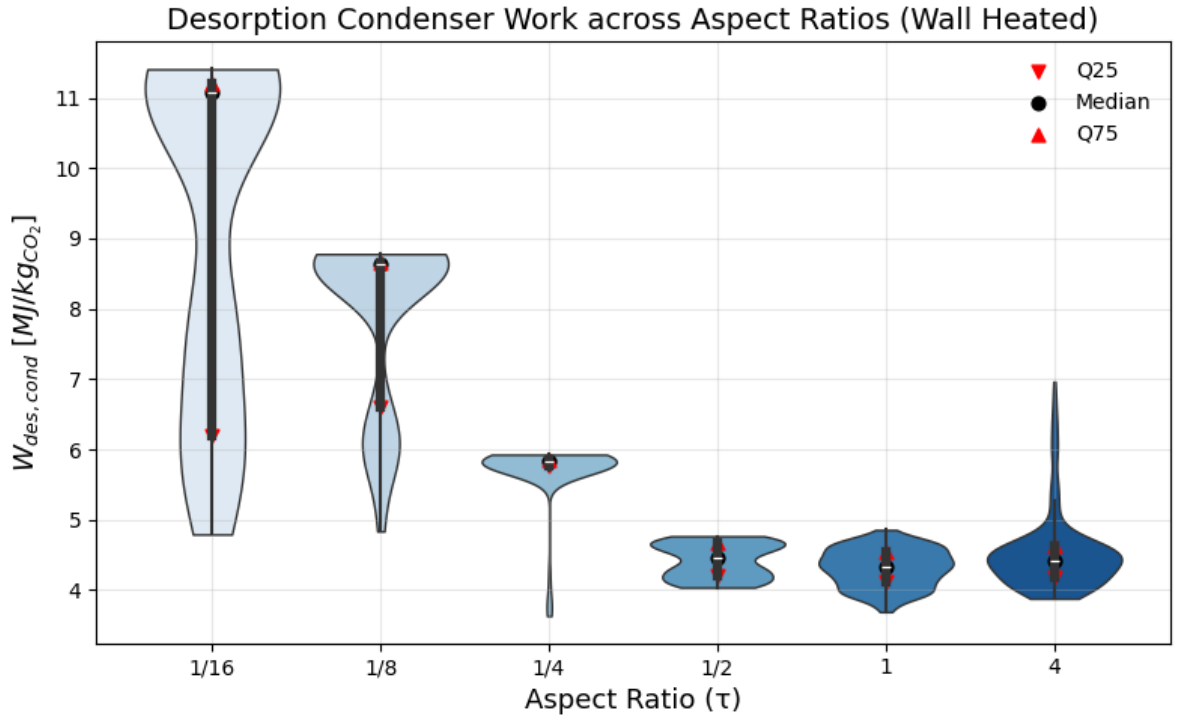

Figure S24: Wall-heated condenser energy distribution.

S4.3 Steam-assisted Pareto-front distributions

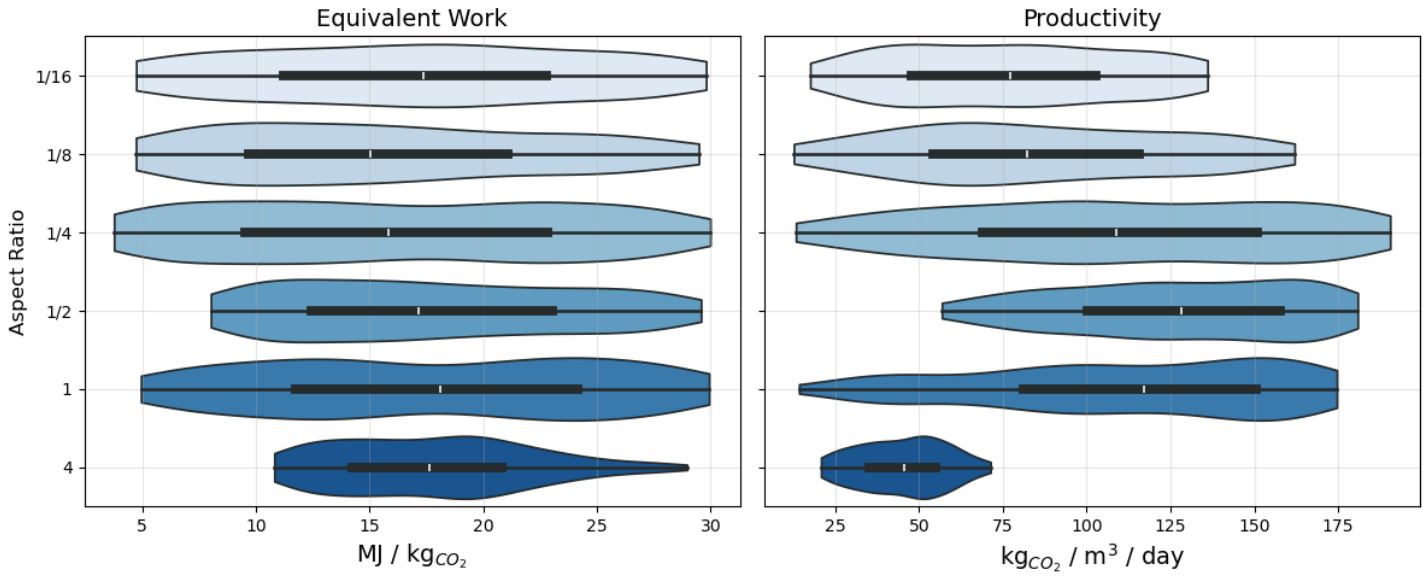

Figure S25: Distribution of Pareto-optimal solutions in the steam-assisted configuration. Left: Violin plots of equivalent work distributions for different aspect ratios. Right: Violin plots of productivity distributions for different aspect ratios.

Unlike the wall-heated case, the distribution of Pareto-optimal solutions is not clustered around a single dominant operating point, but instead appears more homogeneously spread across the productivity–work space. This indicates that in the steam-assisted configuration the trade-off between productivity and equivalent work is less sharply constrained by geometry, and multiple operating regimes can yield comparable performance. As a consequence, marginal and joint mode analyses cannot be meaningfully applied here.

S4.4 Step durations for steam-assisted configuration

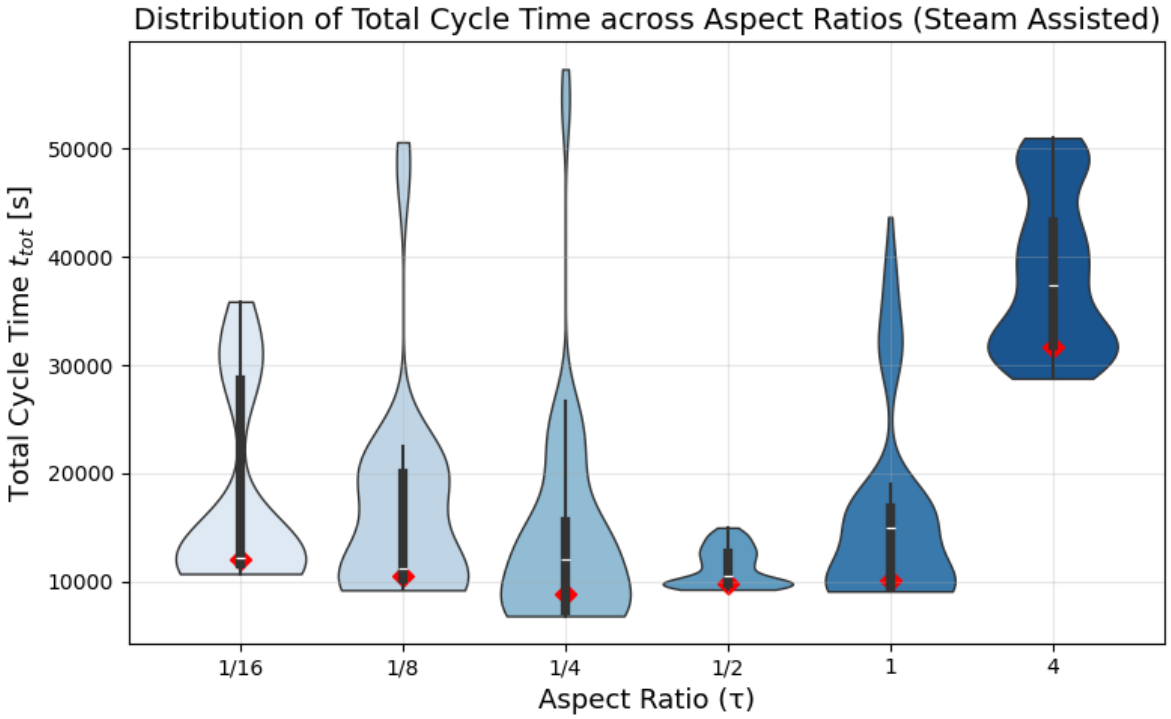

Figure S26: Steam-assisted total cycle-time distribution.

References

S1. John Young, Enrique García-Díez, Susana Garcia, and Mijndert Van Der Spek. The impact of binary water–CO 2 isotherm models on the optimal performance of sorbent-based direct air capture processes. *Energy & Environmental Science*, 14 (10):5377–5394, 10 2021. ISSN 17545706. doi: 10.1039/D1EE01272J. URL https://pubs.rsc.org/en/content/articlehtml/2021/ee/d1ee01272j.

S2. Kagei Seiichiro Wakao Noriaki. *Heat and mass transfer in packed beds*, volume 1. Taylor & Francis, 1982.

S3. J. M.P.Q. Delgado. A critical review of dispersion in packed beds. *Heat and Mass Transfer/Waerme- und Stoffuebertragung*, 42(4):279–310, 2 2006. ISSN 09477411. doi: 10.1007/S00231-005-0019-0/TABLES/6. URL https://link.springer.com/article/10.1007/s00231-005-0019-0.

S4. Anthony G. Dixon and David L. Cresswell. Theoretical prediction of effective heat transfer parameters in packed beds. *AIChE Journal*, 25(4):663–676, 1979. ISSN 15475905. doi: 10.1002/AIC.690250413.

S5. Anthony G. Dixon. An improved equation for the overall heat transfer coefficient in packed beds. *Chemical Engineering and Processing: Process Intensification*, 35 (5):323–331, 10 1996. ISSN 0255-2701. doi: 10.1016/0255-2701(96)80012-2.

S6. M. Díaz-Heras, J. F. Belmonte, and J. A. Almendros-Ibáñez. Effective thermal conductivities in packed beds: Review of correlations and its influence on system performance. *Applied Thermal Engineering*, 171:115048, 5 2020. ISSN 1359-4311. doi: 10.1016/J.APPLTHERMALENG.2020.115048.

S7. P. Zehner and E. U. Schlünder. Wärmeleitfähigkeit von Schüttungen bei mäßigen Temperaturen. *Chemie Ingenieur Technik*, 42(14):933–941, 7 1970. ISSN 1522-2640. doi: 10.1002/CITE.330421408. URL https://onlinelibrary.wiley.com/doi/full/10.1002/cite.330421408https://onlinelibrary.wiley.com/doi/abs/10.1002/cite.330421408https://onlinelibrary.wiley.com/doi/10.1002/cite.330421408.

S8. Bert Koning. Heat and Mass Transport in Tubular Packed Bed Reactors at Reacting and Non-Reacting Conditions. Technical report, University of Twente, Enschede, 10 2002. URL http://www.tup.utwente.nl/catalogue/book/index.jsp?isbn=903651813x.

S9. R. Byron Bird, Warren E. Stewart, and Edwin N. Lightfoot. *Transport Phenomena*. John Wiley & Sons, 2nd edition edition, 2002. ISBN 0-471-41077-2.

S10. The NIST WebBook. URL https://webbook.nist.gov/.

S11. May Yin Ashlyn Low, David Danaci, Hassan Azzan, Robert T. Woodward, and Camille Petit. Measurement of Physicochemical Properties and CO2, N2, Ar, O2, and H2O Unary Adsorption Isotherms of Purolite A110 and Lewatit VP OC 1065 for Application in Direct Air Capture. *Journal of Chemical and Engineering Data*, 68 (12):3499–3511, 12 2023. ISSN 15205134. doi: 10.1021/ACS.JCED.3C00401. URL https://doi.org/10.1021/acs.jced.3c00401.

S12. Bruce E Poling, John M Prausnitz, John P O'connell, New York, Chicago San, Francisco Lisbon, London Madrid, Mexico City, Milan New Delhi, and San Juan. *The properties of gas and liquids*. McGraw-Hill Education, 2001. ISBN 0071499997. doi: 10.1036/0070116822.

S13. Thomas F Edgar, Richard M Felder, John McKenna, Ronald W Rousseau, and Richard C Seagrave. *Multicomponent Mass Transfer*. Wiley Series in Chemical Engineering, 1993.

S14. Sebastian Bruhn Petersen, Eliana Maria Lozano Sánchez, and Thomas Helmer Pedersen. Impact of adsorption kinetics on the integration of temperature vacuum swing adsorption-based direct air capture (TVSA-DAC) with e-methanol production. *Sustainable Energy & Fuels*, 9(3): 879–890, 1 2025. ISSN 2398-4902. doi: 10.1039/D4SE01395F. URL `https://pubs.rsc.org/en/content/articlehtml/2025/se/d4se01395fhttps://pubs.rsc.org/en/content/articlelanding/2025/se/d4se01395f`.

S15. Adam Ward, Maria M. Papathanasiou, and Ronny Pini. The impact of design and operational parameters on the optimal performance of direct air capture units using solid sorbents. *Adsorption*, 30(7):1829–1848, 10 2024. ISSN 15728757. doi: 10.1007/S10450-024-00526-Y/FIGURES/9. URL `https://link.springer.com/article/10.1007/s10450-024-00526-y`.

S16. M. J. Bos, T. Kreuger, S. R.A. Kersten, and D. W.F. Brilman. Study on transport phenomena and intrinsic kinetics for CO2 adsorption in solid amine sorbent. *Chemical Engineering Journal*, 377:120374, 12 2019. ISSN 1385-8947. doi: 10.1016/J.CEJ.2018.11.072.

S17. The Atmosphere — National Oceanic and Atmospheric Administration, 7 2024. URL `https://www.noaa.gov/jetstream/atmosphere`.

S18. Jhon Carrol, Jhon Slupski, and Alan Mather. The Solubility of Carbon Dioxide in Water at Low Pressure. *Journal of Physical and Chemical Reference Data*, 20(6), 6 1991.